Linking neuronal avalanches with oscillatory and broadband $1/f$ activities in the resting human brain

Damián Dellavale[a,*], Giovanni Rabuffo[b,1], Emahnuel Troisi Lopez[c], Antonella Romano[d], Pierpaolo Sorrentino[b,e,f,1,*]

[a] *Consejo Nacional de Investigaciones Científicas y Técnicas (CONICET), Centro Atómico Bariloche, R8402AGP, San Carlos de Bariloche, Río Negro, Argentina.*
[b] *Institut de Neurosciences des Systèmes, Aix-Marseille Universitè, Marseille, France.*
[c] *Institute of Applied Sciences and Intelligent Systems, National Research Council (CNR), 80078, Pozzuoli, Italy.*
[d] *University of Naples Parthenope, Department of Motor Science and Wellness, Naples, Italy.*
[e] *Deparment of Biomedical Science, University of Sassari, Sassari, Italy.*
[f] *Institute of Applied Sciences and Intelligent Systems, National Research Council (CNR), Naples, Italy.*

Abstract

Objective:
Brain oscillations, broadband $1/f$ activity and neuronal avalanches (NA) are valuable conceptualizations extensively used to interpret brain data, yet, these perspectives have mainly progressed in parallel with no current consensus on a rationale linking them. This study aims to reconcile these viewpoints using source-reconstructed MEG data obtained in healthy humans during eyes-closed resting state.
Methods:
We analyzed NA in source-reconstructed MEG data from 47 subjects. For this, we introduced custom measures and a comprehensive array of features characterizing the statistical, spatiotemporal and spectral properties of NA. By using the complex baseband representation of signals we provide an analytical description of the mechanisms underlying the emergence of NA from the Fourier spectral constituents of the brain activity.
Results:
The observed NA disclose a significant spectral signature in the alpha band, suggesting that the large-scale spreading of alpha bursts occurs mainly via brain avalanches. Besides, the NA detected in our MEG dataset can be segregated based on their spectral signature in two main groups having different propagation patterns, where cluster 2 avalanches is mainly related to the spread of

[*] Corresponding authors.
Email addresses: `dellavale@cab.cnea.gov.ar` (Damián Dellavale), `pierpaolo.sorrentino@univ-amu.fr` (Pierpaolo Sorrentino)
[1] Co-last authors.

narrowband alpha bursts across the brain network, whereas cluster 1 avalanches correspond to more spatially localized fluctuations promoted by the broadband $1/f$ activity. We also provide an analytical framework for the evidence showing that a) spectral group delay consistency in specific narrow frequency bands, b) transient cross-regional coherent oscillations and c) broadband $1/f$ activity, are all key ingredients for the emergence of realistic avalanches.
Significance:
The proposed analytical arguments, supported by extensive model and experimental evidence, show how NA emerge from narrowband oscillations and broadband arrhythmic activity co-existing in the human brain. Our results suggest that large-scale spreading of specific narrowband oscillations takes place in a transient manner mainly via NA, which may play a functional role as a long-range interaction mechanism in the resting human brain.

Keywords: human MEG, neuronal avalanches, brain oscillations, broadband $1/f$ activity, group delay, complex baseband representation

---

Highlights

- Neuronal avalanches propagating across the brain during spontaneous resting state activity, are highly structured in terms of their spatial, temporal and spectral properties.
- The link between local above-threshold fluctuations and oscillations can be understood in terms of the group delay consistency across the spectral components of the neuronal activity (spectral group delay consistency).
- Spectral group delay consistency, transient cross-regional coherent oscillations and broadband $1/f$ activity, are all key ingredients for the emergence of realistic avalanches.
- Observed neuronal avalanches can be segregated based on their spectral signature in two main groups having different propagation patterns, where cluster 2 avalanches is specifically related to the spread of narrowband alpha bursts across the brain network, whereas cluster 1 avalanches correspond to more spatially localized fluctuations promoted by the broadband $1/f$ activity.
- Large-scale spreading of alpha bursts occurs mainly via brain avalanches, which may play a functional role as a long-range interaction mechanism in the resting human brain.

1. INTRODUCTION

The human brain generates complex behaviors from the coordinated interaction of neuronal populations, with evidence showing different degrees of

specialization/distribution of these networks. Such coordination is accompanied (or driven) by neural activity patterns that can be measured using techniques like electroencephalography (EEG) or magnetoencephalography (MEG). In general, brain signals are characterized by both narrowband rhythmic (i.e., oscillations) and broadband arrhythmic (i.e., $1/f$ spectral profile) components [1]. Oscillatory neural activity consists of rhythmic (i.e., periodic) fluctuations in the brain's signals, which occur across various narrow frequency bands and have been associated with specific cognitive functions [2]. For example, the alpha rhythm, typically between 8-13 Hz, emerges during closed-eyes wakefulness [3, 4, 5], while the gamma rhythm, exceeding 30 Hz, has been proposed to play a role in higher cognitive processes[6]. These oscillatory components manifest as "bumps" in the signals' Power Spectral Density (PSD). In contrast to brain oscillations, broadband arrhythmic neural activity exhibits a more complex and irregular nature, often associated with scale-free dynamics (i.e., no characteristic temporal scale) [1]. It generally displays a $1/f$ decay pattern in the PSD, featuring a fractal-like distribution of power across frequencies. This broadband noise-like activity contributes significantly to the brain's overall signal and is intricately linked with cognitive processes, potentially carrying valuable information [7]. Traditionally, the study of brain *narrowband oscillations* and *broadband* $1/f$ *activity* has provided two lenses through which electrophysiological data have been examined [8]. In general, spectral attributes like power and phase offer rich insights into brain dynamics, enabling the discrimination of brain activity during perceptual tasks and distinguishing between healthy and pathological dynamics in resting states [9]. Besides narrowband oscillations and broadband $1/f$ activity, the analysis of collective brain dynamics reveals that system-level neuronal activity is interspersed by *salient network events*. During these events, subsets of brain regions collectively exhibit rare fluctuations above a threshold (e.g., signal amplitude > 3 standard deviations), igniting from specific brain sites, propagating across the brain circuitry in an avalanche-like cascade of activations, and finally decaying below the threshold. For this reason, these salient network events are sometimes referred to as neuronal avalanches. Neuronal avalanches occur aperiodically and are consistently observed across imaging modalities, including multielectrode array recordings [10, 11], EEG [12, 13], MEG [12, 14], SEEG [15, 16], fMRI [17], and calcium imaging [18, 19]. Neuronal avalanches have drawn considerable interest due to their potential significance in information processing [20, 21], facilitating responses with a wide dynamical range [22, 23], and playing a role in achieving flexible dynamics [24, 25, 26]. These events were largely studied in the context of the "critical brain hypothesis", which posits that the brain might be operating near a critical point (i.e., at the edge of a phase transition). In fact, neuronal avalanches display hallmark properties expected in systems that self-organize at a critical point, such as the power-law distribution of avalanche durations (life span) and sizes (number of regions recruited) [12, 14, 27]. For the sake of generality, in this manuscript, we will refer to *salient network events*, or *neuronal avalanches* interchangeably, without implying a connection to the brain criticality hypothesis. While narrowband oscillations, broadband $1/f$ ac-

tivity, and neuronal avalanches offer valuable conceptualizations to interpret brain data, these well-established perspectives have mainly progressed in parallel, with only limited literature linking them [28, 29, 30]. Given the ubiquitous and concurrent presence of oscillations, broadband $1/f$ activity, and neuronal avalanches in the brain during rest, a fundamental question arises: Can we establish a connection between these perspectives? In other words, can we invoke a parsimonious explanation that justifies the simultaneous presence of these phenomena? This study aims to reconcile these viewpoints by studying the relation between narrowband oscillations, broadband $1/f$ activity, and neuronal avalanches in source-reconstructed MEG data where healthy participants are recorded during eyes-closed resting state. In this condition, the characteristic alpha peak and $1/f$ decay in the PSD are observed in brain signals, concurrently with neuronal avalanches.

2. METHODS

2.1. Participants and data

In this study we analyzed a source-reconstructed MEG dataset previously published in [31, 25]. In short, 58 young adults (32 males/26 females, mean age $\pm$ SD was 30.72 $\pm$ 11.58) were recruited from the general community. All participants were right-handed and native Italian speakers. The inclusion criteria were (1) no major internal, neurological, or psychiatric illnesses; and (2) no use of drugs or medication that could interfere with MEG/MRI signals. The study complied with the Declaration of Helsinki and was approved by the local Ethics Committee. All participants gave written informed consent. The details regarding the MRI acquisition are described in [31]. All technical details in connection with the MEG device are reported in [32]. MEG pre-processing and source reconstruction were performed as in [31, 25]. Briefly, the MEG registration was divided into two eyes-closed segments of 3:30 min each. To identify the position of the head, four anatomical points and four position coils were digitized. Electrocardiogram (ECG) and electro-oculogram (EOG) signals were also recorded. The MEG signals, after an anti-aliasing filter, were acquired at 1024 Hz, then a fourth-order Butterworth IIR band-pass filter in the 0.5-48 Hz band was applied. Principal component analysis was used to remove environmental noise measured by reference magnetometers. Supervised independent component analysis was adopted to clean the data from physiological artefacts, such as eye blinking (if present) and heart activity (generally one component). Noisy channels were identified and removed manually by an expert rater (136 $\pm$ 4 sensors were kept). After this pre-processing, 47 subjects were selected for this work and all further analyses were conducted on signal amplitudes of 1 min in duration source-reconstructed to 84 brain regions of interest (BROI) based on the Desikan-Killiany-Tourville (DKT) anatomical parcellation atlas.

2.2. Avalanches detection

To estimate neuronal avalanches we first detected the local above-threshold fluctuations. That is, the source-reconstructed time series of each brain re-

gion was discretized in amplitude by computing the z-score, then positive and negative excursions beyond a threshold were identified. The value of the amplitude threshold was set to three standard deviations ($\pm 3\sigma$ or equivalently $|z| = 3$). Then the avalanches duration was assessed by considering that a neuronal avalanche begins when, in a sequence of contiguous time bins, at least one brain region is active ($|z| > 3$) and ends when all the brain regions are inactive ($|z| \leq 3$) [10, 14]. Besides, the avalanche size was defined as the total number of active brain regions during a given avalanche. In this work, we analyzed *neuronal avalanches*, also referred through the manuscript as *salient network events*, without implying a connection to the brain criticality hypothesis [31].

2.3. Avalanches activation and co-activation matrices

For each detected avalanche, we computed the activation matrix (brain regions $\times$ time bins) as follows. The source-reconstructed, z-scored and time binned signal were binarized, such that, at any time bin, a brain region exceeding ± 3 was set to 1 (active), and all other regions were set to 0 (inactive, see Figure 2C). For each detected avalanche, we also computed the co-activation matrix (brain regions $\times$ brain regions) by assigning 1 to all the brain regions recruited in that particular avalanche. Thus, the diagonal of the co-activation matrix contains 1s in all the brain regions active during a given avalanche. Besides, summation across rows (or columns) produce, in each brain region, the number of co-activated regions during a given avalanche (i.e., in terms of graph theory, this is known as the degree of each brain region). The mean co-activation matrix shown in the Figure 6C was computed by first averaging the co-activation matrices corresponding to all the neuronal avalanches detected in each subject, and then, averaging the resulting matrix across all the participants.

2.4. Avalanches spatiotemporal profile

To characterize avalanches spatiotemporal profile, we introduce two BROI-wise metrics: The *mean avalanche duration* measuring the typical duration of neuronal avalanches propagating through a brain region; and the *mean avalanche spatial extension* measuring the typical size of avalanches propagating through a brain region. Specifically, we assign to each brain region the mean avalanche duration (or size) computed on all the avalanches recruiting that particular region. The *mean avalanche duration* and *mean avalanche spatial extension* profiles shown in the Figures 1E,G were computed by first considering all the neuronal avalanches detected in each subject, and then, averaging the resulting profiles across all the participants.

2.5. Avalanche spectral matrix

For the spectral characterization of neuronal avalanches we introduce the Avalanche Spectral Matrix (ASM). To obtain the ASM we first compute the whitened time-frequency representation on the whole time series of each brain region (see Figure 2E). Then, the whitened time-frequency maps were selectively averaged across the time points corresponding to the occurrence of the neuronal

avalanche of interest. As a result, we obtain a whitened power spectrum (see Figure 2F) associated with each brain region conforming the ASM (Brain regions $\times$ Frequency bins) for that particular neuronal avalanche. The time-frequency maps were computed as scalograms using Morlet wavelets including spectral whitening by Z_{H0}-score normalization of each frequency bin across time samples as in [33]. The ASM can be defined at the single avalanche level (see Figure 2G), by averaging all the avalanches in each subject (data not shown) and by averaging the mean ASM of each subject across all the participants (see Figures 2H and 3A,B). To assess the statistical significance of the spectral signatures associated with the neuronal avalanches, we compute pixel-level thresholding on the mean ASM with Bonferroni correction for multiple comparisons. More specifically, we computed the mean ASM on each one of the 100 B- or C-surrogate datasets (see Section 2.9). Then these 100 surrogate mean ASMs were used to compute pixel-level thresholding on the true mean ASM using a Bonferroni-adjusted two-tailed statistical threshold = 0.05/(Brain regions $\times$ Frequency bins). Note that this Bonferroni correction for multiple comparisons assuming independence between adjacent spatial/frequency bins of the mean ASM is a quite conservative test, yet, the observed spectral signature in the alpha band result evident even after this stringent thresholding process (see Figure 2H).

2.6. Avalanches waveform shape

To characterize the waveform shape of neuronal avalanches we follow a BROI-wise approach. First, in each brain region we computed the average across the 200 ms signal epochs (absolute value) centered around the start time of the avalanches of interest recruiting that particular region (see gray lines in Figures 3C,D and B.11C,D). Then, we obtained the mean avalanches waveform shape by computing the average of the resulting time series across the brain regions (see the red and blue lines in Figures 3C,D and B.11C,D).

2.7. Avalanches propagation modes

To assess the avalanches starting modes we assign to each brain region the number of avalanches igniting in that particular site (e.g., see the brain region active at $Time \approx 51.581$ sec in the activation matrix shown in Figure 2C). Similarly, for the avalanches ending modes we assign to each brain region the number of avalanches extinguishing in that particular site (e.g., see the brain region active at $Time \approx 51.597$ sec in the activation matrix shown in Figure 2C). For the avalanches maximum recruitment modes we assign to each brain region the number of avalanches involving that particular site during the avalanche maximum size (e.g., see the 4 brain regions active at $Time \approx 51.591$ sec in the activation matrix shown in Figure 2C). Last, by dividing the avalanche count obtained in each brain region by the total number of processed avalanches, we obtained the mean spatial profiles for the starting, maximum recruitment and ending avalanches modes as shown in the Figures B.8 and B.12.

2.8. Clustering of avalanches

Neuronal avalanches were clustered according to their spectral signature by using the Louvain method for community detection based on modularity maximization [34, 35]. First, the Matrix of Paired Distance (MPD) was obtained by computing the Euclidean distance between the vectorized ASMs corresponding to the neuronal avalanches of interest taken in pairs. The resulting MPD (Avalanches $\times$ Avalanches) was normalized to be in the range $[0, 1]$, and the Adjacency Matrix (AM) was computed as $\mathrm{AM} = 1 - \mathrm{MPD}$. Then, the Louvain algorithm was repeated 100 times on the AM for resolution parameter values in the range $0.5 \leq \gamma \leq 2$ [34, 36]. Optimization of modularity quality function, based on the maximization of the similarity measure (z-scored Rand index) [36], was achieved for resolution parameter values within the range $0.9 \lesssim \gamma \lesssim 1.1$. Finally, a consensus partition was found from the 100 partitions [37, 38, 39]. For the avalanches detected in our source-reconstructed MEG dataset, the Louvain algorithm consistently identified two avalanche clusters with significant differences in terms of mean avalanche duration, size and spectral signature in their mean ASM (see Figures 3, B.10 and B.11).

2.9. Surrogate datasets

We generated phase-randomized A-surrogate datasets, that preserve the PSD in each brain region, while disrupting the phase relationships of the spectral components (both within and between brain regions). For this, in each brain region we implemented a frequency domain randomization procedure, which involves taking the Discrete Fourier Transform (DFT) of the time series, adding a random phase-shift in the range $[-\pi, \pi]$ on each spectral component of the DFT (preserving the odd phase symmetry associated with real signals [40]), and then taking the inverse DFT to obtain the surrogate signal back in the time domain [41]. The 100 phase-randomized A-surrogate datasets were obtained by applying this procedure 100 times on each brain region independently. In addition, we also generated B-surrogate datasets that randomize the phases similarly to the A-surrogate, but in this case preserving both the regional PSDs and the cross-spectra. For this, we follow a similar procedure as described above with the difference that the same random phase-shift was applied to all the brain regions. This implies that the phase difference between any pair of brain regions in *homologous frequency components* is preserved (i.e., preservation of cross-spectra). This corresponds to preserving the Pearson's correlations between brain regions (see Appendix A.1). However, the B-surrogates destroy the phase relationships between *non-homologous frequency components*. Finally, we generated 100 C-surrogate sets of avalanches by randomizing the starting time of each observed avalanche and keeping unaltered all the other properties like the avalanche duration and brain regions involved in each avalanche.

2.10. Spectral group delay consistency measures

In Appendix A.2 we introduce the pairwise complex baseband representation of band-limited signals (eqs. A.7 - A.10 and A.13 - A.16) to provide analytical

arguments showing that the link between local above-threshold fluctuations and oscillations can be understood in terms of the group delay consistency across the spectral components (i.e., Fourier oscillatory constituents) of the neuronal activity. The spectral group delay associated with the activity of the brain region r, is defined as the rate of change of the phase $\phi_r(\omega)$ with the frequency ω computed on the Fourier spectrum of the brain activity (i.e., the DFT): $\tau_r(\omega) = -\Delta\phi_r(\omega)/\Delta\omega(\omega)$. Where the incremental phase $\Delta\phi_r(\omega)$ is defined as the phase difference between spectral components (adjacent in frequency ω) constituting the neural activity of the brain region r. The theoretical analysis presented in Appendix A.2 suggests that the spectral group delay consistency (SGDC) is an important feature linking the oscillatory properties of a signal to the above-threshold fluctuations associated with neuronal avalanches. For an in-depth and more mathematically rigorous description of the oscillatory mechanisms eliciting above-threshold fluctuations in the brain signals and the measures quantifying the SGDC, the reader is referred to Appendix A.2 and Appendix A.3. Here, we briefly introduce the SGDC measures designed to efficiently quantify this feature in experimental data as follows,

$$SGDC(r) = \frac{1}{N} \sum_{\omega} e^{-i\Delta\phi_r(\omega)} : \Delta\omega = \text{cte. across } r \tag{1}$$

$$SGDC(\omega) = \frac{1}{N} \sum_{r} e^{-i\Delta\phi_r(\omega)} : \Delta\omega = \text{cte. across } \omega \tag{2}$$

Equations 1 and 2 define the SGDC measures as the Euler transformed incremental phase values $\Delta\phi_r(\omega)$ averaged across the spectral components or brain regions, respectively, with N being the number of either frequency values or brain regions as appropriate. Importantly, the $SGDC(r)$ measure (Equation 1) assesses the emergence of local above-threshold fluctuations from the spectral components constituting the activity of the brain region r, whereas the $SGDC(\omega)$ measure (Equation 2) quantifies the synchronization of the above-threshold oscillatory bursts at the frequency ω across brain regions. We also define the pairwise spectral group delay consistency (pSGDC) to quantify the burstiness and cross-regional bursts synchronization in a single measure.

$$pSGDC(r_1, r_2) = \underbrace{\left(\frac{SGDC(r_1) + SGDC(r_2)}{2}\right)}_{\text{Mean pairwise burstiness}} \underbrace{\frac{1}{N} \sum_{\omega} e^{-i(\Delta\phi_1(\omega) - \Delta\phi_2(\omega))}}_{\text{Correlation of burstiness across } \omega} : \Delta\omega = \text{cte. across } r \tag{3}$$

Equation 3 shows that $pSGDC(r_1, r_2)$ is a linear measure conformed by a factor quantifying the cross-regional correlation between the group delays across the frequency values, weighted by a coefficient quantifying the burstiness of the two involved brain regions (r_1, r_2). Unless otherwise specified the SGDC and pSGDC measures were computed on the whole time series of each brain region (i.e., non-time-resolved approach). That is, we first obtain the phase values corresponding

to the Fourier spectral components by computing the DFT (via the Fast Fourier Transform algorithm) on the whole time series of each brain region. Then, SGDC and pSGDC measures were computed on the incremental phase $\Delta\phi_r(\omega)$ obtained as the phase difference between the Fourier spectral components taken in adjacent pairs across the frequency ω. In particular, this non-time-resolved approach was used to produce the results shown in the Figures 6 and B.9. On the other hand, in Figure B.10 we follow a time-resolved approach. That is, the $SGDC(\omega)$ array was computed in each detected avalanche by considering the brain regions and time interval associated with each particular avalanche. Then, the $SGDC(\omega)$ arrays were averaged selectively across the avalanches segregated in the two clusters produced by the Louvain algorithm (see Section 2.8 and Figure B.10).

3. RESULTS

3.1. Statistical, spatiotemporal, and spectral characterization of neuronal avalanches

We identified neuronal avalanches in our dataset and studied their characteristic signatures. In particular, we introduced a comprehensive array of features describing the statistical, spatiotemporal and spectral properties of neuronal avalanches. Traditionally, neuronal avalanches are described in terms of the distribution of their sizes and durations, which follow fat-tailed distributions (Figures 1A,C). The study of these distributions is generally used to assess the dynamical regime where the brain dynamics are idling (often implied to be around a critical point). However, it is also informative to describe how neuronal avalanches propagate through the brain regions of interest (BROI) by assessing their spatial, temporal, and spectral signatures. To characterize the spatiotemporal profiles of avalanches, we introduce two BROI-wise metrics (see Methods, Section 2.4): The *mean avalanche duration* measures the typical duration of neuronal avalanches propagating through a brain region (Figures 1E,F); and the *mean avalanche spatial extension* measures the typical size of avalanches propagating through a brain region (Figures 1G,H). The brain plots in Figures 1F,H reveal a characteristic topography, demonstrating the heterogeneous role that each brain region plays in the propagation of neuronal avalanches. Next, we introduce a tool to characterize the spectral signature of neuronal avalanches, by first transforming the regional signals into a time-frequency representation and then averaging the time-frequency content selectively across the time points corresponding to the occurrence of each neuronal avalanche (Figures 2E,F). This way, we defined the spectral fingerprint of each neuronal avalanche, which we named Avalanche Spectral Matrix (ASM, see Methods). Figure 2 displays the ASM for a single avalanche (panel G) and averaged across all subjects (panel H). Figure 2H shows that the frequency content of most brain regions peaks in the alpha band (8-13 Hz) during neuronal avalanches. In other words, during salient network events, brain regions fluctuate predominantly in alpha. This is also observed away from the occipital regions, suggesting that synchronization

in the alpha band might spread on a large-scale during neuronal avalanches (see in Section 3.6 the discussion of the results shown in Figure B.10). Note that this result provides a relevant insight regarding the connection between salient network events and narrowband oscillations and, it is non-trivial since neuronal avalanches are rare phenomena, occupying only a small fraction of the total recording (in space and time), generally around 1% of time points. The ASM can be defined at the single avalanche level (Figure 2G). Thus, we asked if avalanches with different spectral signatures propagate differently. In particular, we hypothesized a relationship between the avalanche spectral signature (ASMs) and the avalanche duration and extension, as defined above. To test this relationship, we clustered neuronal avalanches according to their ASM using the Louvain algorithm (see Methods). We found that avalanches cluster into two main groups based on their frequency content (Figures 3A,B). Importantly, we found a statistically significant difference of the mean avalanches duration and size between cluster 1 and cluster 2 (see Figures 3E,H). For this, in each brain region we computed a non-parametric permutation test (random sampling without replacement, 1×10^4 permutations). All the brain regions disclosed a statistically significant difference of the mean avalanches duration and size between cluster 1 and 2 (the Bonferroni-adjusted two-tailed P values result $P < 0.001$ in all the brain regions). The avalanches belonging to cluster 1 (Figure 3A) display a less marked and less widespread alpha peak in the ASM as compared to cluster 2 (Figure 3B). Consistently, the two clusters are also well distinguished by their different waveform shapes, with group 1 showing shorter temporal profiles of above-threshold fluctuations. Figures 3C,D show the average waveform shapes of avalanches, obtained by averaging in each brain region (BR) the absolute value of the time series associated with each neuronal avalanche (see Methods). These results suggest that cluster 2 avalanches is specifically related to the long-range spread of narrowband alpha bursts across the brain network, whereas cluster 1 avalanches correspond to more spatially localized fluctuations mainly promoted by the broadband $1/f$ activity (see Figures 3E-J). The two identified clusters are also characterized by different avalanche duration and size, which confirms our hypothesis. In particular, cluster 1 avalanches are generally small and short-lived when compared to cluster 2 avalanches (see Figures 3E,H,G,J), although both clusters display avalanche size and duration distributions spanning across a few orders of magnitude (see Figures 3G,J). Interestingly, the slope of the fat-tailed distributions is different in the two clusters, which could have implications for the study of power-law statistics related to the criticality hypothesis. We also found that avalanches propagate in a cluster-specific manner (see Figure B.8 in Appendix B.2) That is, the spatial profiles associated with the start and end of each avalanche cluster disclose a high correlation between the two clusters (see Figures B.8A-C and Figures B.8G-I), whereas a different scenario is observed in terms of how the brain regions are recruited by the two avalanche clusters. Specifically, brain regions that are recruited by the longer avalanches of cluster 1, will be recruited by the shorter avalanches of cluster 2, and vice versa (see Figure B.8D). Within cluster 1, the longest avalanches occupy the frontal and

occipital regions (see Figure B.8E), whereas in cluster 2, associated with the spectral signature in the alpha band, the longest avalanches are in the parietal and temporal regions (see Figure B.8F). The opposite trend is observed for the shortest avalanches. In fact, performing Pearson's correlations between the spatial profiles of cluster 1 and cluster 2 corresponding to the maximal size of recruitment across brain regions, we obtain a strong negative correlation ($r = -0.841$, $P < 0.001$ two-tailed Student's t-test, see Figure B.8D). Note that the specificity of cluster 2 avalanches, associated with transient above-threshold alpha bursts, in recruiting parietal and temporal brain regions can not be trivially explained by the presence of elevated (steady) alpha oscillatory power, which is commonly observed in occipital brain regions during the eyes-closed resting state (see Figure 2B). In summary, in this section we have introduced a comprehensive array of avalanche features, showing that rare, short-lived salient network events propagating across the brain during spontaneous resting state activity are highly structured in terms of their spatial, temporal, and spectral properties. In particular, the spectral characterization using the ASM provided relevant insights regarding the connection between the observed salient network events and narrowband oscillations in the alpha band.

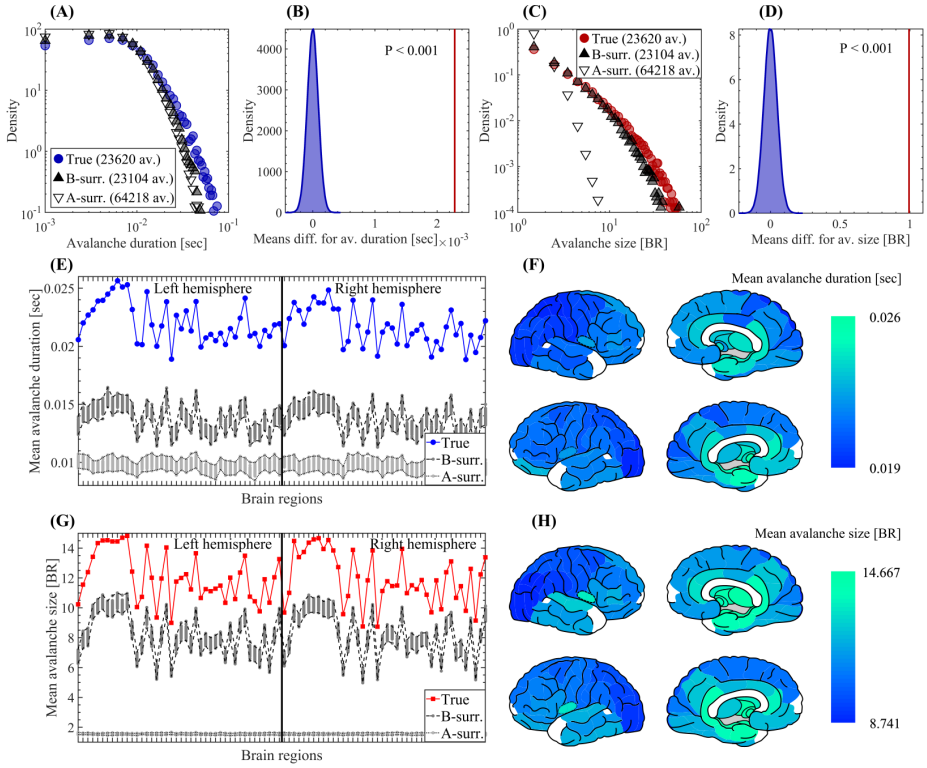

Figure 1: Statistical and spatiotemporal characterization of neuronal avalanches. (A) Distribution of the duration of neuronal avalanches observed in the true source-reconstructed MEG data (filled blue circles), the A-surrogate (empty down-pointing triangles) and the B-surrogate (filled up-pointing triangles). In the three cases the avalanches were computed on the 47 participants. The distributions of avalanches duration for the true MEG data and the B-surrogate disclose a statistically significant difference ($P < 0.001$, two-sample Kolmogorov-Smirnov test). (B) Results of the non-parametric permutation test. Histogram corresponding to the sampling distribution of the difference between the means of the true and B-surrogate distributions of avalanches duration. The histogram was computed via random sampling without replacement (1×10^5 permutations). The red vertical line in the histogram indicates the actual mean difference between the true and B-surrogate distributions of avalanches duration. The two-tailed P value is reported. (C) Same as in A for the size of neuronal avalanches. The distributions of avalanches size for the true MEG data and the B-surrogate disclose a statistically significant difference ($P < 0.001$, two-sample Kolmogorov-Smirnov test). (D) Same as in B for the size of neuronal avalanches. (E) Spatial profile showing the mean duration of neuronal avalanches propagating through each brain region (mean value across the 47 participants, see Methods). (F) Brain topographies for the mean duration of neuronal avalanches as shown in panel E. (G) Same as in E for the size of neuronal avalanches. (H) Same as in F for the size of neuronal avalanches. Symbols and abbreviations: BR, Brain Regions.

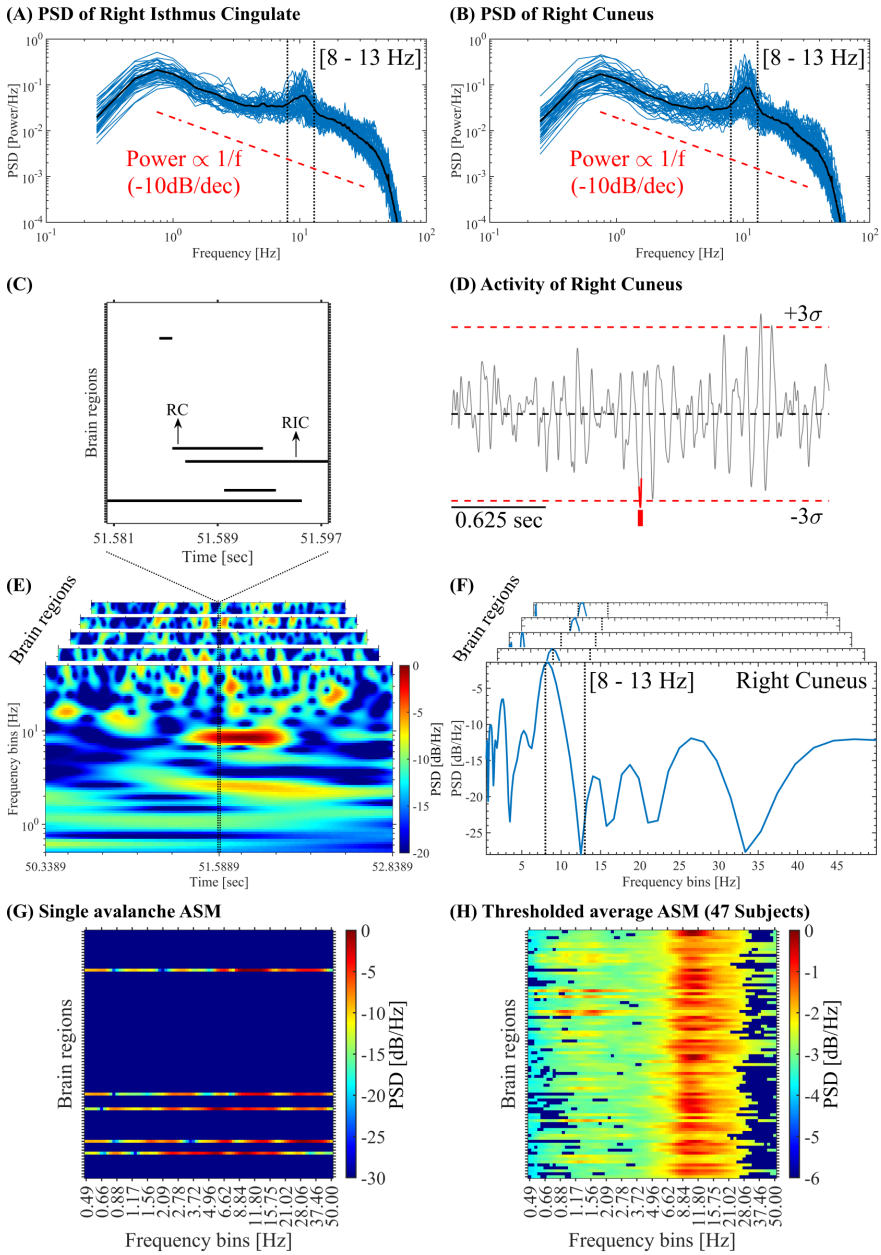

Figure 2: Avalanche Spectral Matrix. (A, B) Power spectra computed on the Right Isthmus Cingulate (RIC, panel A) and the Right Cuneus (RC, panel B) activities (1 min length) of each patient (blue lines) and the resulting average (black line). Note that the PSDs of the RC (panel B) disclose a prominent bump in the alpha band (8-13 Hz) characteristic of the occipital brain regions, however, a less prominent bump in the alpha band is also observed in regions away from the occipital cortex (see the PSDs of RIC shown in panel A). (C) Activation matrix of a single avalanche showing the time intervals in which each brain region was active (i.e., absolute amplitude $> 3\sigma$). (D) Activity of the RC disclosing the above-threshold fluctuation (highlighted in red) associated with the brain avalanche shown in panel C. (E) Whitened time-frequency maps (see Methods) of each brain region involved in the avalanche shown in panel C. (F) Whitened power spectra associated with each brain region involved in the avalanche shown in panel C. The vertical dotted lines indicate the alpha band. To build the ASM, we average the whitened time-frequency content selectively across the time samples corresponding to the occurrence of each neuronal avalanche. As a result, we obtain a whitened power spectrum for each brain region. (G) ASM corresponding to the neuronal avalanche shown in panel C. (H) Mean ASM resulting from the average across all the avalanches detected in the 47 subjects, and then, Bonferroni-thresholded using the B-surrogate (see Methods). Symbols and abbreviations: ASM, Avalanche Spectral Matrix; PSD, Power Spectral Density; RC, Right Cuneus; RIC, Right Isthmus Cingulate.

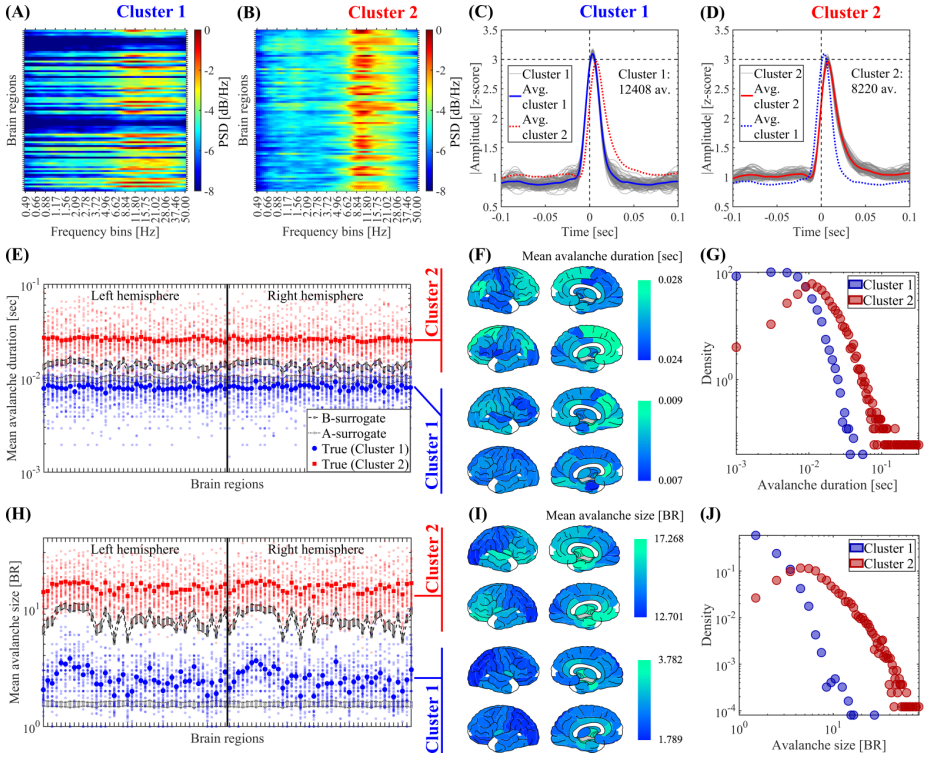

Figure 3: Clustering of avalanches according to spectral signature. The avalanches obtained from 41 subjects were clustered using the Louvain algorithm (resolution parameter $\gamma = 1$, see Methods). (A, B) Mean ASM of the two avalanches clusters identified by the Louvain algorithm computed on the avalanches detected in the 41 participants. (C, D) Waveform shapes of the avalanches pertaining to the two avalanches clusters identified by the Louvain algorithm. Thin gray lines correspond to the average waveform shape in each brain region. Thick blue and red lines correspond to the resulting waveform shape averaged across the brain regions for avalanche cluster 1 and 2, respectively. (E) Spatial profile showing the mean duration of avalanches pertaining to cluster 1 (in blue) and cluster 2 (in red). For the true data, the small and big markers correspond to the mean spatial profile in each patient and the average across the 41 participants, respectively (see Methods). To test the significance of the difference of the mean avalanches duration between cluster 1 and cluster 2, in each brain region we computed a non-parametric permutation test (random sampling without replacement, 1×10^4 permutations). All the brain regions disclosed a statistically significant difference of the mean avalanches duration between cluster 1 and 2 (the Bonferroni-adjusted two-tailed P values result $P < 0.001$ in all the brain regions). (F) Brain topographies for the mean duration of neuronal avalanches averaged across the 41 participants as shown in panel E. (G) Distribution of the duration of avalanches pertaining to the cluster 1 and cluster 2 observed in the 41 participants. (H) Same as in E for the size of neuronal avalanches. To test the significance of the difference of the mean avalanches size between cluster 1 and cluster 2, in each brain region we computed a non-parametric permutation test (random sampling without replacement, 1×10^4 permutations). All the brain regions disclosed a statistically significant difference of the mean avalanches size between cluster 1 and 2 (the Bonferroni-adjusted two-tailed P values result $P < 0.001$ in all the brain regions). (I) Same as in F for the size of neuronal avalanches. (J) Same as in G for the size of neuronal avalanches. Symbols and abbreviations: BR, Brain Regions.

3.2. Neuronal avalanches and phase coherence: surrogate data analysis

During neuronal avalanches, the signals display large deviations from the baseline, which are coordinated across regions, giving rise to complex activation patterns with well-defined statistical, spatiotemporal, and spectral features. In this work, we hypothesize that the presence of narrowband oscillations, broadband $1/f$ activity, and transient synchronization across the spectral components of brain signals, both locally in a region and globally across brain regions, are necessary conditions for the emergence of realistic neuronal avalanches. A common way to test the necessary and/or sufficient conditions underlying a phenomenon (here, neuronal avalanches) is the use of surrogate data analysis. This approach involves creating surrogate datasets that remove or alter a specific property (e.g., phase relationships) while preserving other statistical characteristics, allowing one to determine if the absence or modification of the property affects the observed feature of interest. Following this line of reasoning, we generated 100 phase-randomized "A-surrogate" datasets (see Methods), that preserve the PSD in each brain region, while disrupting the phase relationships of the spectral components (both within and between brain regions). Despite the A-surrogates having the same spectral content as the original data, they do not disclose fat-tailed distributions of avalanche size and duration (see A-surrogates in Figures 1A,C), nor realistic spatiotemporal patterns of propagation (see A-surrogates in Figures 1E,G) and ASMs (data not shown). Another hypothesis to rule out is that the avalanche properties shown in Figure 1 could be ascribed to the static correlations between signals (which are not preserved by the A-surrogates). To test this hypothesis, we generated 100 phase-randomized B-surrogate datasets (see Methods) that randomize the phases similarly to the A-surrogate, but in this case preserving both the regional PSDs and the cross-spectra. The preservation of cross-spectra implies that the phase difference between any pair of brain regions in *homologous frequency components* is preserved. This corresponds to preserving Pearson's correlations between brain regions (see Appendix A.1). However, the B-surrogates destroy the phase relationships between *non-homologous frequency components*. As shown in Figure 1, the observed distributions of avalanches duration and size (Two-sample Kolmogorov-Smirnov test: $P < 0.001$ for panels A and C), mean spatiotemporal properties (see B-surrogates in panels E, G and the results of permutation test shown in panels B and D), and ASMs (see Figure 2H) are not explained by the B-surrogates. Notice that these results are non-trivial, since in both the original and the B-surrogate datasets the number of neuronal avalanches is almost identical, and large events are also observed in the surrogate data (see B-surrogates in Figures 1A,C). To summarize, despite retaining the same power spectra and cross-spectra, the loss of synchronization across spectral components (given by the phase randomization), impairs large-scale coordinated salient network events, significantly disrupting the statistics and features of neuronal avalanches.

3.3. Neuronal avalanches, narrowband oscillations and broadband $1/f$ activity: modeling insights

We built a signal model to elucidate the relation between neuronal avalanches, narrowband oscillations, and broadband $1/f$ activity. We model the activity of single brain regions as the linear superposition of Fourier components oscillating in a narrow frequency band. As a result, the corresponding spectral representation discloses a "bump" of (null-to-null) bandwidth in the alpha band (8-13 Hz, Figures 4A,D,G). The broadband arrhythmic activity was modeled by imposing a $1/f$ trend in the PSD of each signal (Figure 4G). This $1/f$ spectral background was chosen to mimic the $-10dB/dec$ log-log decay rate observed in the PSDs associated with true data (see Figures 2A,B). To model different degrees of phase coherence, we assign random phase values to the spectral components within a range $[-\epsilon\pi, \epsilon\pi]$ with $\epsilon \in [0, 1]$ (see right panels in Figures 4A,D,G). On the one hand, for $\epsilon \simeq 1$, the spectral components of the signal were desynchronized (i.e., independent oscillatory components, Figure 4A). On the other hand, for $\epsilon \simeq 0$ the spectral components were highly synchronized (i.e., high cross-frequency coherence). We first focused on a *single brain signal* and measured the number of salient events (i.e., transient excursions of the amplitude above a fixed threshold of 3 standard deviations: $\pm 3\sigma$) depending on the presence or absence of coherent oscillations and $1/f$ activity (see Figures 4C,F,I). In the absence of $1/f$ activity and for uniformly distributed random phases assigned to the spectral components in the alpha band ($\epsilon = 1$, Figures 4A), the model displays very few above-threshold fluctuations across trials (Figures 4B,C). Increasing the coherence of the spectral components in the alpha band ($\epsilon = 0.75$, Figures 4D), despite the absence of $1/f$ activity, the number of above-threshold fluctuations increased, producing a salient burst in most of the trials (Figures 4E,F). Finally, the presence of the broadband $1/f$ activity with $\epsilon = 1$ and coherent spectral components in the alpha band with $\epsilon = 0.75$ (Figure 4G) further increased the number of salient events in a single brain signal (Figures 4H,I). Importantly, the $1/f$ activity also influences the rhythmicity of above-threshold fluctuations, which occur aperiodically. More specifically, if we synthesize a long time series by concatenating trials constructed without the $1/f$ activity (as in Figures 4E), the concatenated time series will disclose a periodic series of above-threshold alpha bursts (i.e., one salient alpha burst per trial). Instead, in the presence of $1/f$ activity we obtain above-threshold fluctuations occurring at random in each trial besides the salient alpha burst, hence, the time series resulting from concatenating trials (as in Figure 4H) will disclose an aperiodic series of above-threshold fluctuations. In summary, these results suggest that the mere presence of oscillations associated with an increase of power around a narrow frequency band does not guarantee the stable occurrence of above-threshold fluctuations (Figures 4A-C). However, if the phases of the spectral components are coherent, then high-amplitude fluctuations are consistently observed in the signal (Figures 4D-F). Furthermore, a specific relationship between the amplitudes of the narrowband oscillations and the broadband arrhythmic component is necessary for the resulting local activity to exhibit realistic aperiodically occurring above-threshold fluctuations (see regime R2 in Figure 4I).

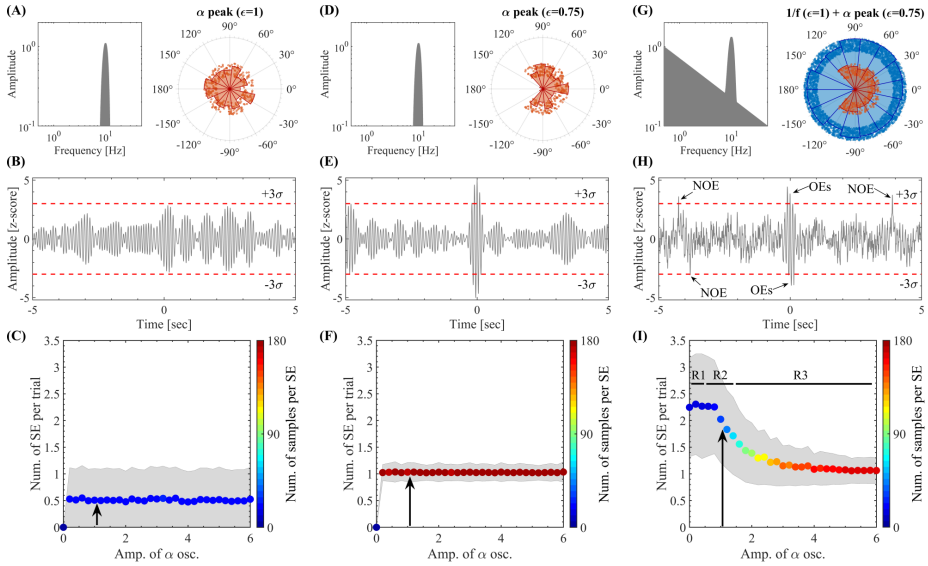

Figure 4: Model for local above-threshold fluctuations. (A) Amplitude spectrum (left) and distribution of the phase values assigned to the spectral components (right) for the oscillatory activity in the alpha band (Hann window with null-to-null bandwidth = 8-13 Hz, frequency resolution $df = 1/60\text{sec} \approx 0.017$ Hz). Random phases were assigned to all the spectral components within the range $[-\epsilon\pi, \epsilon\pi]$ with a phase factor $\epsilon = 1$. (B) 10 sec epoch extracted from the synthetic time series produced by the amplitude spectrum and phase distribution shown in panel A (sampling rate of $f_s = 1024$ Hz). The horizontal dashed lines in red indicate the 3 standard deviations ($\pm 3\sigma$) thresholds used to compute the salient events as above-threshold amplitude fluctuations. (C) Number of salient events (SE) per trial as a function of the maximum amplitude of the oscillatory activity in the alpha band. For each maximum amplitude value, we counted the number of SE across 1000 trials of 10 sec in length (trials) synthesized as the one shown in panel C. In each trial, we recomputed the random phases of the spectral components within the range $[-\epsilon\pi, \epsilon\pi]$ with $\epsilon = 1$. The colored markers indicate the mean number of SE per trial across the 1000 trials. The shaded error bars in gray correspond to the standard deviation around the mean value. The pseudocolor scale represents the mean value for the number of above-threshold samples per salient event. The black arrow indicates the maximum amplitude of the alpha oscillations used in panels A and B. (D-F) Same as in A-C for spectral components with random phases constrained within the range $[-\epsilon\pi, \epsilon\pi]$ with $\epsilon = 0.75$ (see the distribution of the phase values in panel D). (G) Amplitude spectral profile (left) resulting from the linear superposition of 1) a narrowband amplitude spectrum around the alpha band (Hann window with null-to-null bandwidth = 8-13 Hz), and 2) a set of spectral components with power $A^2(f) \propto 1/f$ (frequency resolution $df = 1/60\text{sec} \approx 0.017$ Hz). The right side of panel G shows the distribution of phase values assigned to the spectral components. Random phases within the range $[-\epsilon\pi, \epsilon\pi]$ with $\epsilon = 1$ where assigned to the spectral components constituting the $1/f$ background (blue circles) and $\epsilon = 0.75$ where assigned to the spectral components associated with the alpha bump (red circles). (H) Same as in B and E for the spectrum shown in panel G. In this case, it is possible to distinguish oscillatory (OEs) and non-oscillatory (NOEs) salient events. R1, R2 and R3 indicate regions characterized by *Amp. of alpha oscillations* less than, approx. equal to and greater than the *Amp.* $1/f$ *activity*, respectively. Symbols and abbreviations: SE, Salient Events.

Next, we extended the above setup to model *whole-brain activity* and neuronal avalanches. For each simulated brain signal, we set the amplitude of the

alpha peak proportionally to that observed in empirical MEG recordings (with alpha amplitude $\in [0, 1]$), thus modeling the non-homogeneous presence of alpha activity across brain regions. In addition, in each region, we bounded the random phases assigned to the spectral components in the alpha band within a range $[-\epsilon\pi, \epsilon\pi]$, whose width $\epsilon \in [0.75, 1]$ was inversely proportional to the empirical alpha power (i.e., the higher the alpha peak, the higher the phase coherence among the spectral components). This choice was motivated by the fact that high PSD bumps are generally interpreted as stronger narrowband synchronization within local neuronal populations [42] (see Discussion). Using this setup, we measured synthetic neuronal avalanches and tested their dependence on the $1/f$ activity. When only alpha oscillations were present, and no broadband $1/f$ activity (Figure 5A), the ASM was not realistic compared to the empiric one (Figure 5B), and the distribution of avalanche durations and sizes was not following a linear trend in log-log plots (Figures 5C,D). Instead, when only broadband $1/f$ activity was present, and no oscillatory activity in the alpha band nor coherent phase values were used (i.e., $\epsilon = 1$; Figure 5E), the ASM did not show the spectral signature associated with the alpha component (Figure 5F). Also, the distribution of avalanche durations was similar to the empirical data, while the distribution of avalanche sizes was shrunk, as the model did not display events involving large populations (Figures 5G,H). Finally, when both broadband $1/f$ activity and alpha oscillations were simultaneously present (Figure 5I), the emerging neuronal avalanches displayed a realistic ASM (compare Figure 5J with Figures 2H) as well as fat-tailed distributions of durations and sizes (Figures 5K,L); although the sizes decayed in a markedly more rapid fashion than in the empirical data (compare Figures 5K,L with Figures 1A,C). These results suggest that both narrowband oscillations and broadband $1/f$ spectral background contribute to the signal deviations from baseline activity and realistic neuronal avalanches, provided that the narrowband spectral components display appropriate levels of phase coherence.

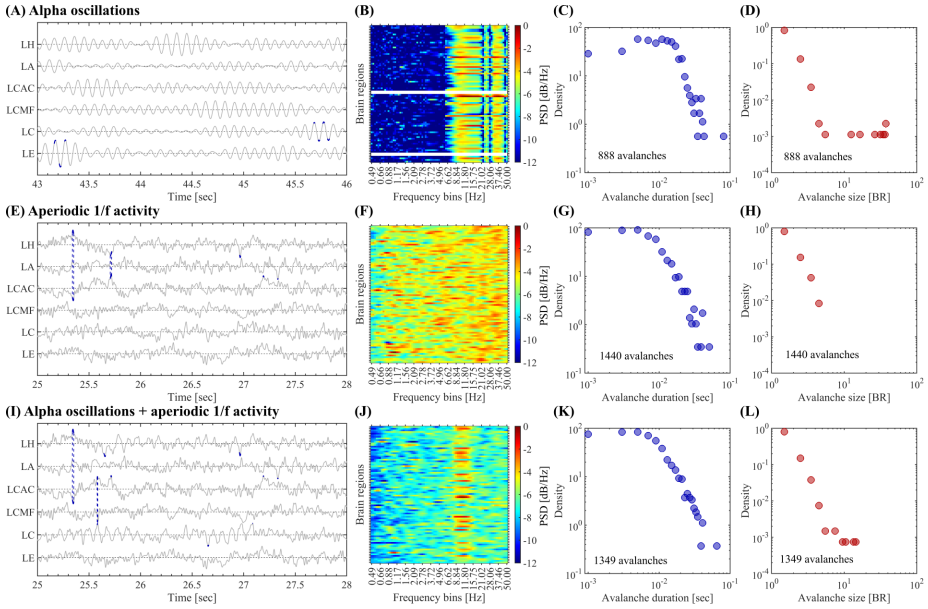

Figure 5: Large-scale model for neuronal avalanches. (A-D) Large-scale model for neuronal avalanches including only alpha oscillations (random phase values in the alpha band constrained to the range $[-\epsilon\pi, \epsilon\pi]$ with $\epsilon \in [0.75, 1]$). Panel A shows a subset of synthetic activities. In each time series, the above-threshold fluctuations ($\pm 3\sigma$) are highlighted in dark blue. Vertical dashed lines connect the activations constituting avalanches completely contained in the subset of signals shown. Panel B shows the resulting ASM averaged across the avalanches. Panels C and D show the distribution of avalanche duration and size, respectively. Panels A-C were computed on all the avalanches detected in a simulated time series of 1 min in length. (E-H) Same as in A-D for the large-scale model including only broadband $1/f$ activity, and no oscillatory activity in the alpha band nor phase consistency values were present ($\epsilon = 1$). (I-L) Same as in A-D for the large-scale model including both broadband $1/f$ activity with non-constrained random phases ($\epsilon = 1$) and alpha oscillations with random phases constrained proportionally to the observed alpha power in the range ($\epsilon \in [0.75, 1]$). Symbols and abbreviations: LH, Left Hippocampus; LA, Left Amygdala; LCAC, Left Caudal Anterior Cingulate; LCMF, Left Caudal Middle Frontal; LC, Left Cuneus; LE, Left Entorhinal.

3.4. Spectral group delay consistency underlies local above-threshold fluctuations

In the present and the next sections, we provide a unifying rationale for the mechanisms underlying the empiric and model evidence presented in Sections 3.1, 3.2 and 3.3. Here, we present the analytical arguments showing that the link between local above-threshold fluctuations and oscillations can be understood in terms of the group delay consistency across the spectral components constituting the brain activity. In particular, we found that the magnitude of the phase factor ϵ, associated with the results shown in Figure 4, creates above-threshold fluctuations by affecting the spectral group delay $\tau(\omega) \approx -\Delta\phi(\omega)/\Delta\omega$, defined as the rate of change of the phase $\phi(\omega)$ with the frequency ω computed on the Fourier spectrum of the brain activity (i.e., the DFT). We studied this phenomena using both numerical (Figures B.6 and B.7) and analytically tractable

(Figures A.1 and A.2) modeling examples. For the analytical approach, we used the complex baseband representation of signals based on grouping the Fourier spectral components in (non-overlapping) pairs adjacent in frequency. In this representation, the time series of interest is decomposed as a linear superposition of amplitude modulated components (see Figures A.1E,J and A.2E,J and the synthesis equations A.7 - A.10 and A.13 - A.16). Essentially, when all the Fourier spectral components are added together to synthesize the signal in the time domain (i.e., the inverse DFT), the spectral group delay determines the time alignment of the amplitude envelope associated with each pair of adjacent spectral components (see the amplitude modulated components in Figures A.1E,J and A.2E,J). Such time alignment promotes transient large-amplitude excursions of the signal (i.e., above-threshold fluctuations). Specifically, for adjacent spectral components having highly dissimilar phase values disclosing a nonlinear dependence with the frequency ω (e.g., random phase values with $\epsilon \simeq 1$ as shown in the right panel of Figure 4A), the resulting spectral group delay depends on ω (see Figures A.1H and A.2H). In this case, we say that the signal has low spectral group delay consistency (SGDC) which reduces the occurrence of above-threshold fluctuations (see Figures A.1J and A.2J). Instead, in the case of adjacent frequency bands with phase values depending linearly with ω or having phase values disclosing a nonlinear dependence with ω but constrained within a small phase range (e.g., random phase values with $\epsilon \simeq 0.75$ as shown in the right panel of Figure 4D), we obtain approximately constant group delay values for all the pairs of adjacent spectral components (see Figures A.1C and A.2C). In such a case, the signal has a high SGDC which promotes the occurrence of above-threshold fluctuations (see Figures A.1E and A.2E). The numerical results shown in the Figure B.6 confirm these findings in the case of the signal model for local above-threshold fluctuations. Specifically, Figure B.6 shows that the increase of the signal burstiness, as quantified by the kurtosis, associated with more constrained random phase values (i.e., low phase factor ϵ values) is explained by the increase in the SGDC as quantified by the $SGDC(r)$ measure. Importantly, we re-compute the signal model for the same set of phase factor values used in Figure B.6, this time using spectral phase values disclosing not a random but a linear dependence with the frequency (i.e. a time-shift). The results obtained with this configuration are shown in Figure B.7. As predicted by the spectral group delay mechanism (see Figures A.1A-E), we obtained $|SGDC(r)| \approx 1$ independently of the phase factor value ($\epsilon \in [0, 1]$), and the time series produced by the signal model disclosed (time-shifted) above-threshold fluctuations in all the cases (see Figure B.7). These numerical results constitute further evidence showing that the SGDC effectively underlies the emergence of local above-threshold fluctuations from narrowband oscillations. For an in-depth and more mathematically rigorous description of this mechanism, the reader is referred to Appendix A.2. To quantitatively study the effects of SGDC on our data we introduce specialized measures (see Methods and Appendix A.3). The $SGDC(r)$ is bounded in the range $[0, 1]$ and quantifies how much the group delay varies across the spectral components associated with the signal of interest (see Equation 1). In Appendix A.3 we show the performance of

the $SGDC(r)$ measure in assessing the emergence of local above-threshold fluctuations from the Fourier oscillatory components of synthetic signals (see Figure A.3). Importantly, we found that the $SGDC(r)$ measure discloses a significant positive correlation with the number of observed above-threshold fluctuations ($r = 0.184$, $P < 0.001$ two-tailed Student's t-test, see Figure B.9G), implying that in our MEG dataset a significant fraction of the local salient events are above-threshold oscillatory bursts associated with high SGDC (mainly in the alpha band). Taken together, these results suggest that the emergence of local above-threshold fluctuations from the Fourier oscillatory constituents of the brain activity can be understood in terms of the SGDC as quantified by the $SGDC(r)$ measure.

3.5. Spectral group delay consistency, transient cross-regional coherent oscillations and broadband $1/f$ activity underlie neuronal avalanches

In Sections 3.3 and 3.4, we have shown that the concurrent presence of broadband $1/f$ activity and narrowband oscillations disclosing appropriate levels of SGDC, are two key ingredients sufficient to generate realistic above-threshold fluctuations in a single brain signal. In this section, we present the rationale and results pointing out that SGDC is a key conceptualization also in connection with the emergence of realistic neuronal avalanches as a collective phenomena involving multiple brain regions. Firstly, in Appendix A.4 we provide a theoretical approach showing that the data-driven results presented in Section 3.2 associated with the A- and B-surrogates can be understood in terms of SGDC properties. We analytically found that, despite of preserving the power spectrum (which includes alpha oscillations and broadband $1/f$ activity), the phase randomization associated with both A- and B-surrogates significantly reduces the burstiness of each brain region (i.e., occurrence of above-threshold fluctuations) as assessed by the $SGDC(r)$ measure (see Appendix A.4). This reduction in the $SGDC(r)$ magnitude provides a theoretical argument underpinning the evidence showing that A- and B-surrogates failed to reproduce realistic neuronal avalanches (see Section 3.2). Moreover, our empirical results show that A-surrogates perform worst than B-surrogates in reproducing realistic neuronal avalanches (see Figure 1). This evidence is consistent with the analytical derivations presented in Appendix A.4 showing that B-surrogates preserve the original magnitude of the $SGDC(\omega)$ measure, and only A-surrogates destroy both the burstiness of each brain region (as assessed by the $SGDC(r)$ measure) and the synchronization of above-threshold fluctuations across brain regions (as assessed by the $SGDC(\omega)$ measure). Secondly, the spectral signature in the alpha band disclosed by the averaged ASMs associated with the neuronal avalanches observed in our MEG data (see Figure 2H), suggests that coherence in the alpha band occurring in a transient manner across brain regions is also an essential feature of the realistic avalanches. To test this, we generated 100 C-surrogate sets of avalanches (see Methods) that randomize the starting time of each observed avalanche and keep unaltered all the other properties like the time width and brain regions involved in each avalanche. Figures B.10A and B.10B show

the average ASMs corresponding to the true and C-surrogate avalanches computed on 10 subjects, respectively. In particular, Figure B.10B shows that the alpha signature is barely distinguishable in the average ASM corresponding to the C-surrogate avalanches. Importantly, as shown in the Figure B.10C, the average ASM of the true avalanches thresholded with the average ASM of the C-surrogate avalanches (see Methods) discloses a prominent spectral signature in the alpha band. As a conclusion, these results suggest that the large-scale spreading of alpha bursts occurs mainly via brain avalanches. Although the $SGDC(r)$ measure assesses the emergence of above-threshold fluctuations from the Fourier oscillatory constituents of the activity associated with a single brain region, it does not account for cross-regional effects associated with neuronal avalanches. To quantitatively study the cross-regional effects of SGDC on our data we introduce the $SGDC(\omega)$ measure. The $SGDC(\omega)$ is bounded in the range $[0, 1]$ and quantifies how much the group delay at a given frequency ω varies across brain regions (see Equation 2). In Appendix A.3 we show the performance of the $SGDC(\omega)$ measure in assessing the emergence of above-threshold fluctuations synchronized across brain regions (see Figures A.4 and A.5). Figures B.10D and B.10E show the average ASMs of the two avalanche clusters identified by the Louvain algorithm (see Methods) computed on 10 subjects. Importantly, the Figure B.10F shows the increase of transient cross-regional coherence around the alpha band, as quantified by the $SGDC(\omega)$ measure, associated with the avalanches disclosing the alpha spectral signature in the average ASM (i.e., avalanche cluster 2). Notably, Figure B.10G shows that the transient cross-regional coherence around the alpha band associated with the cluster 2 avalanches is also captured by the large-scale model presented in Section 3.5. In summary, these results suggest that a) spectral group delay consistency in specific narrow frequency bands (as assessed by the $SGDC(r)$ measure), b) transient cross-regional coherent oscillations (intra-frequency coherence across brain regions assessed by the $SGDC(\omega)$ measure) and c) broadband $1/f$ activity, are all key ingredients for the emergence of realistic avalanches.

3.6. Mechanisms of long-range interactions

Synchrony is thought to play a role in coordinating information processing across different brain regions. However, correlation structures such as hemodynamic functional connectivity are better explained in terms of power amplitude correlations of electrophysiological signals (e.g., MEG), rather than phase-synchrony. In a recent work, it was demonstrated that power correlation between two signals can be analytically decomposed into signal coherence (a measure of phase synchronization), cokurtosis (a measure of the probability of simultaneous large fluctuations), and conjugate-coherence [43]. In particular, it was proposed that the cokurtosis between two signals provides a measure of co-bursting that offers a robust neurophysiological correlate for hemodynamic resting-state networks [43]. Here we show that the SGDC conceptualization can be used to explain both the co-burstiness and the cokurtosis in terms of the coherence of the signals' spectral content, therefore, advancing our understanding of the mechanisms of long-range communication. For this, we counted

the co-participation of pairs of brain regions across avalanches (see Methods, Section 2.3). Figure 6C shows the number of co-activations between each pair of brain regions. Figure 6B shows the number of relative co-activations, i.e., the accumulated number of activations in each row of the co-activation matrix relative to the total number of activations in each brain region (diagonal of the co-activation matrix). Figure 6A displays the brain plots corresponding to the number of relative co-activations shown in Figure 6B. It is essential to note that the topography of co-activations shown in the Figures 6A-C can not be trivially explained by the chance co-occurrence of rare above-threshold fluctuations in the brain activity. In fact, Figure B.9 shows that even though the kurtosis (Equation A.25) and the $SGDC(r)$ (Equation 1) are highly correlated with the emergence of local salient events (see Figures B.9C,G), they fail to reproduce the topography of co-activations associated with the observed neuronal avalanches (compare Figures 6A,B with Figures B.9A,B,E,F and see the regressions in Figures B.9D,H). Of note, the $SGDC(r)$ measure essentially quantifies the presence of above-threshold bursts mainly associated with SGDC in the alpha band, whereas kurtosis assesses the presence of both oscillatory and non-oscillatory above-threshold fluctuations (outliers in the tails of the distribution of amplitude values). To account for both the burstiness and cross-regional bursts synchronization we used the pairwise SGDC measure (pSGDC). The $pSGDC(r_1, r_2)$ is defined as a factor quantifying the cross-regional correlation between the group delays across the frequency values, weighted by the average $SGDC(r)$ of each pair of signals r_1 and r_2 (see Equation 3 in Methods and Equations A.23 and A.24 in Appendix A.3). Figures 6D-F show that the profile of co-bursting across brain regions, as quantified by the $pSGDC(r_1, r_2)$ measure, significantly correlates with the observed co-activations topography and also generates statistics that are lost in the A- and B-surrogates. In our MEG dataset we found that, similarly to the pSGDC measure, the cokurtosis, as defined in the Equation A.26, also correlates with the observed co-activations topography and generates statistics that are lost in the A- and B-surrogates (see Figures 6G-I). Linear correlations: Co-activations vs pSGDC, $r = 0.390$, $P < 0.001$ (Figure 6F). Co-activations vs Cokurtosis, $r = 0.388$, $P < 0.001$ (Figure 6I). Co-activations vs Pairwise Pearson's correlation, $r = 0.252$, $P = 0.021$ (data not shown). The statistical significance of these linear correlations was assessed by using the Student's t distributions of the two-tailed hypothesis test under the null hypothesis that the correlation is zero. Of note, the pSGDC measure quantifies the co-occurrence of above-threshold bursts mainly associated with SGDC in the alpha band, whereas cokurtosis assesses the presence of both oscillatory and non-oscillatory co-burstiness across brain regions. Importantly, the analysis proposed here based on the $SGDC(r)$, $SGDC(\omega)$ and $pSGDC(r_1, r_2)$ measures, admits relevant mechanistic interpretations linking the Fourier oscillatory constituents of the brain activity and neuronal avalanches. Specifically, the avalanches co-activation pattern reproduced by the pSGDC measure (see Figures 6A-F) can be mechanistically segregated in two components: 1) the results associated with the $SGDC(r)$ measure (Figures B.9E-H) supporting the emergence of local above-threshold fluctuations via SGDC mainly in the alpha band,

and 2) the results associated with the $SGDC(\omega)$ measure (Figure B.10F) supporting the co-occurrence of above-threshold alpha bursts across brain regions (i.e., transient cross-regional coherence around the alpha band). The component 1 can be interpreted as an entraining mechanism producing transient synchronizations of the oscillatory activity of neuronal populations around specific frequency bands (local cross-frequency synchronization), whereas the component 2 can be associated with a long-range interaction via transient cross-regional coherence in narrowband oscillations.

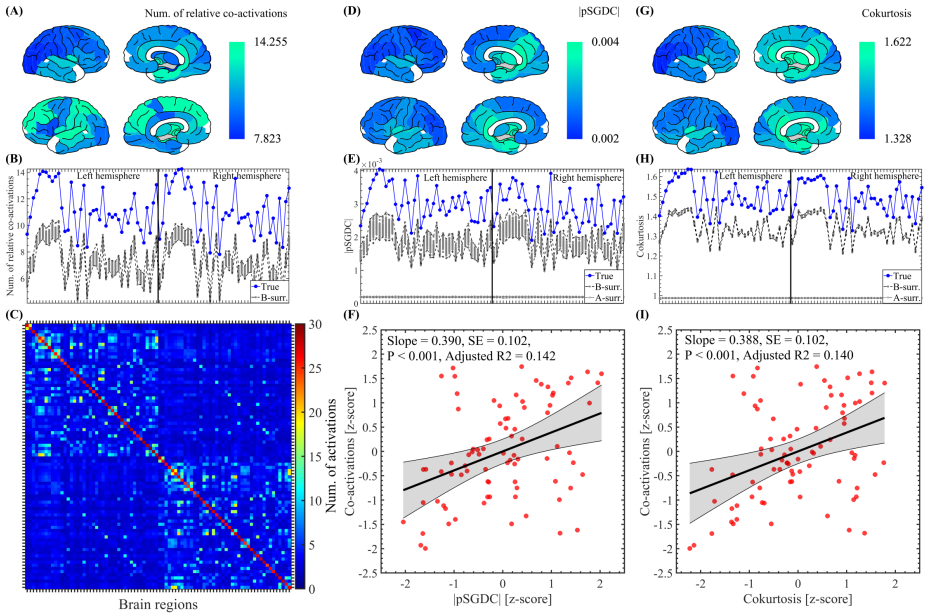

Figure 6: Co-activation pattern of brain avalanches compared against pSGDC and cokurstosis measures computed on whole time series of the brain regions taken in pairs. (A) Brain topographies corresponding to the co-activation profile shown in panel B (blue markers). (B) Spatial profile showing the number of relative co-activations (mean value across the 47 participants), i.e., the accumulated number of activations in each row of the co-activation matrix relative to the total number of activations in each brain region (diagonal of the co-activation matrix). (C) Co-activation matrix averaged across the brain avalanches observed in the 47 participants (see Methods). (D-E) Same as in A-B for the pSGDC measure. (F) Scatter plot showing the correlation between the co-activation and pSGDC spatial profiles shown in panels B and E, respectively. Number of samples (red circles) = Number of brain regions = 84. The thick black line and black shaded error bars represent the linear regression and the 95% confidence interval, respectively. The reported P value for the statistical significance of the linear regression was assessed using Student's t distributions of the two-tailed hypothesis test under the null hypothesis that the correlation is zero. (G-I) Same as in D-F for the cokurtosis measure.

4. DISCUSSION

Frequency-domain representation of brain signals, via Fourier transforms (e.g., DFT), have been extensively used for decades in many neuroscience fields

to analyze the neural activity across several spatiotemporal scales. Regardless of the functional significance of neural oscillations, if any, the Fourier basis functions provide an arguably good characterization of the rhythmic components observed in the brain activity. In this study, we used the complex baseband representation of signals, based on the Fourier theory, to analytically define the spectral group delay consistency (SGDC) as a novel conceptualization linking brain avalanches with the signals' spectral content. Importantly, the SGDC framework allowed us to provide a unifying rationale for the emergence of local salient events and neuronal avalanches from the Fourier oscillatory constituents of the brain activity. First, the analytical arguments described in Appendix A.2 point out that in order to observe realistic local above-threshold fluctuations, the spectral components constituting the brain signals must disclose a certain degree of cross-frequency coherence as assessed by the $SGDC(r)$ measure (see Figures 4A-C, 4D-F, B.6, B.7, A.1 and A.2). Second, we analytically showed that A- and B-surrogates failed to reproduce realistic neuronal avalanches mainly because the phase randomization reduces the SGDC across both frequency bands and brain regions which impairs a) the burstiness of each signal (occurence of above-threshold fluctuations) and b) the synchronization of above-threshold fluctuations across brain regions, respectively (see Section 3.5 and Appendix A.4). Third, the spectral signature in the alpha band disclosed by the averaged ASM of cluster 2 avalanches constitutes relevant evidence linking the observed brain avalanches with narrowband oscillations. Importantly, this feature associated with the synchronization of above-threshold alpha bursts across brain regions can be explained in terms of the SGDC mechanism through the $SGDC(\omega)$ measure (see Figures B.10F,G and Sections 3.5 and 3.6). Fourth, the SGDC conceptualization allowed us, via the $pSGDC(r_1, r_2)$ measure, to explain both the co-activation pattern of brain avalanches and cokurtosis in terms of the coherence of the signals' spectral content, therefore, advancing our understanding of the mechanisms of long-range communication. The empiric, modeling and analytical results presented in this work guided us to identify the essential building blocks underlying the emergence of realistic neuronal avalanches as observed in our MEG dataset, which can be summarized as follows:

1 Spectral group delay consistency. This feature explains the emergence, in a single brain region (i.e., locally), of transient above-threshold fluctuations associated with an specific frequency band (e.g., alpha bursts). The SGDC (e.g., bounded phase differences across spectral components associated with the alpha peak) can be interpreted as an entraining mechanism producing transient synchronizations of the oscillatory activity of neuronal populations around specific frequency bands. We note that bounded phase differences across spectral components might be produced by neuronal populations that are communicating locally, under the communication-through-coherence (CTC) hypothesis.

2 Transient cross-regional coherent alpha oscillations. This feature explains the transient synchronization of the above-threshold alpha bursts across brain regions, giving rise to the neuronal avalanches producing the alpha spec-

tral signature in the ASM (i.e., avalanche cluster 2). This type of neuronal avalanches can be putatively associated with a long-range interaction mechanism through specific narrowband oscillations taking place in a transient manner (i.e., transient CTC).

3 Broadband $1/f$ activity. This feature explains the emergence of non-oscillatory above-threshold fluctuations occurring in an aperiodic manner, mainly associated with the short-lived avalanches with no characteristic spectral signature in the ASM (i.e., avalanche cluster 1). The close relationship between avalanche cluster 1 and the $1/f$ spectral features implies that this type of avalanches could play a more local role linked to either local excitation-inhibition balance or to critical dynamics [7].

Linking the presence of neuronal avalanches to the group delay consistency across the Fourier oscillatory components of the brain activity is a relevant result of this study implying that avalanches might mediate interactions across both frequency bands and brain regions as discussed above. In this regard, the CTC hypothesis posits that neural communication is facilitated by the presence of synchronized (steady) oscillations across brain regions. Our results extend the CTC hypothesis by showing that long-range interaction through specific narrowband oscillations may take place in a transient manner via neuronal avalanches (i.e., transient CTC). Indeed, the results presented in the Figure B.10 suggest that the large-scale spreading of alpha bursts occurs mainly via brain avalanches. As a result, this evidence suggests that transient cross-regional coherence associated with the occurrence of neuronal avalanches disclosing the spectral signature in the alpha band (i.e., avalanche cluster 2), may play a functional role as a long-range interaction mechanism in the resting human brain. One of the main limitations of this study is related to the uncertain capability of our dataset to accurately identify deep brain sources along the cortical surface, mainly due to the ill-posed nature of the source-reconstructed MEG data. In order to address this issue, we re-computed the analysis of avalanches presented in this work, but this time excluding the deep sources. It was found that all the conclusions and, in particular, all the characteristics of the observed neuronal avalanches remain essentially unaltered when the deep sources are excluded from the avalanche analysis (See Figures B.11 and B.12 in Section Appendix B.3).

5. CONCLUSION

In this work we provided a detailed analytical description of the mechanisms underlying the emergence of neuronal avalanches from narrowband oscillations and broadband arrhythmic activity co-existing in the human brain. The proposed analytical arguments were tested and confirmed using local and large-scale models together with experimental data (MEG recordings obtained in healthy subjects during closed-eyes resting state). We also discussed the evidence in connection with the large-scale spreading of alpha bursts associated with the occurrence of neuronal avalanches, as a long-range interaction mechanism in the resting human brain.

ACKNOWLEDGEMENTS

REFERENCES

[1] B. J. He, Scale-free brain activity: past, present, and future, Trends Cogn Sci 18 (9) (2014) 480–487. doi:10.1016/j.tics.2014.04.003.

[2] György Buzsáki, Rhythms of the Brain, Oxford University Press, 2006.

[3] H. Berger, Über das Elektrenkephalogramm des Menschen, Archiv F Psychiatrie 87 (1929) 527–570. doi:10.1007/BF01797193.

[4] E. D. Adrian, B. H. C. Matthews, The Berger rhythm: Potential changes from the occipital lobes in man, Brain 57 (1934) 355–385. doi:10.1093/brain/57.4.355.

[5] S. Palva, P. J. M., New vistas for alpha-frequency band oscillations, Trends in Neurosciences 30 (2007) 150–158. doi:10.1016/j.tins.2007.02.001.

[6] C. A. Bosman, C. S. Lansink, C. M. Pennartz, Functions of gamma-band synchronization in cognition: from single circuits to functional diversity across cortical and subcortical systems, Eur J Neurosci 39 (2014) 1982–1999. doi:10.1111/ejn.12606.

[7] A. Nanda, G. W. Johnson, Y. Mu, M. B. Ahrens, C. Chang, D. J. Englot, M. Breakspear, M. Rubinov, Time-resolved correlation of distributed brain activity tracks E-I balance and accounts for diverse scale-free phenomena, Cell Rep 42 (112254). doi:10.1016/j.celrep.2023.112254.

[8] M. Gerster, G. Waterstraat, V. Litvak, K. Lehnertz, A. Schnitzler, E. Florin, G. Curio, V. Nikulin, Separating Neural Oscillations from Aperiodic 1/f Activity: Challenges and Recommendations, Neuroinform 20 (2022) 991–1012. doi:10.1007/s12021-022-09581-8.

[9] C. Keitel, M. Ruzzoli, L. Dugué, N. A. Busch, C. S. Y. Benwell, Rhythms in cognition: The evidence revisited, Eur J Neurosci 55 (2022) 2991–3009. doi:10.1111/ejn.15740.

[10] J. M. Beggs, D. Plenz, Neuronal avalanches in neocortical circuits, J Neurosci 23 (2003) 11167–11177. doi:10.1523/JNEUROSCI.23-35-11167.2003.

[11] J. M. Beggs, D. Plenz, Neuronal avalanches are diverse and precise activity patterns that are stable for many hours in cortical slice cultures, J Neurosci 24 (2004) 5216–5229. doi:10.1523/JNEUROSCI.0540-04.2004.

[12] J. M. Palva, A. Zhigalov, J. Hirvonen, O. Korhonen, K. Linkenkaer-Hansen, S. Palva, Neuronal long-range temporal correlations and avalanche dynamics are correlated with behavioral scaling laws, Proc Natl Acad Sci U S A 110 (2013) 3585–3590. doi:10.1073/pnas.1216855110.

[13] G. M. Duma, A. Danieli, G. Mento, V. Vitale, R. S. Opipari, V. Jirsa, P. Bonanni, P. Sorrentino, Altered spreading of neuronal avalanches in temporal lobe epilepsy relates to cognitive performance: A resting-state hdEEG study, Epilepsia 64 (2023) 1278–1288. doi:10.1111/epi.17551.

[14] O. Shriki, J. Alstott, F. Carver, T. Holroyd, R. N. Henson, M. L. Smith, R. Coppola, E. Bullmore, D. Plenz, Neuronal avalanches in the resting MEG of the human brain, J Neurosci 33 (2013) 7079–7090. doi:10.1523/JNEUROSCI.4286-12.2013.

[15] V. Priesemann, M. Valderrama, M. Wibral, M. Le Van Quyen, Neuronal avalanches differ from wakefulness to deep sleep-evidence from intracranial depth recordings in humans, PLoS Comput Biol 9 (e1002985). doi:10.1371/journal.pcbi.1002985.

[16] A. Zhigalov, G. Arnulfo, L. Nobili, S. Palva, J. M. Palva, Relationship of fast- and slow-timescale neuronal dynamics in human MEG and SEEG, J Neurosci 35 (2015) 5385–5396. doi:10.1523/JNEUROSCI.4880-14.2015.

[17] E. Tagliazucchi, P. Balenzuela, D. Fraiman, D. R. Chialvo, Criticality in large-scale brain fMRI dynamics unveiled by a novel point process analysis, Front Physiol 3. doi:10.3389/fphys.2012.00015.

[18] M. Yaghoubi, T. de Graaf, J. G. Orlandi, F. Girotto, M. A. Colicos, J. Davidsen, Neuronal avalanche dynamics indicates different universality classes in neuronal cultures, Sci Rep 8 (3417). doi:10.1038/s41598-018-21730-1.

[19] Z. Bowen, D. E. Winkowski, S. Seshadri, D. Plenz, P. O. Kanold, Neuronal Avalanches in Input and Associative Layers of Auditory Cortex, Front Syst Neurosci 13. doi:10.3389/fnsys.2019.00045.

[20] W. L. Shew, H. Yang, S. Yu, R. Roy, D. Plenz, Information capacity and transmission are maximized in balanced cortical networks with neuronal avalanches, J Neurosci 31 (2011) 55–63. doi:10.1523/JNEUROSCI.4637-10.2011.

[21] W. L. Shew, D. Plenz, The functional benefits of criticality in the cortex, Neuroscientist 19 (2013) 88–100. doi:10.1177/1073858412445487.

[22] O. Kinouchi, M. Copelli, Optimal dynamical range of excitable networks at criticality, Nature Phys 2 (2006) 348–351. doi:10.1038/nphys289.

[23] D. B. Larremore, W. L. Shew, J. G. Restrepo, Predicting criticality and dynamic range in complex networks: effects of topology, Phys Rev Lett 106 (058101). doi:10.1103/PhysRevLett.106.058101.

[24] E. Tognoli, J. A. Kelso, The metastable brain, Neuron 81 (2014) 35–48. doi:10.1016/j.neuron.2013.12.022.

[25] P. Sorrentino, R. Rucco, F. Baselice, R. De Micco, A. Tessitore, A. Hillebrand, L. Mandolesi, M. Breakspear, L. Gollo, G. Sorrentino, Flexible brain dynamics underpins complex behaviours as observed in Parkinson's disease, Sci Rep 11 (4051). doi:10.1038/s41598-021-83425-4.

[26] P. Sorrentino, S. Petkoski, M. Sparaco, E. Troisi Lopez, E. Signoriello, F. Baselice, S. Bonavita, M. A. Pirozzi, M. Quarantelli, G. Sorrentino, V. Jirsa, Whole-Brain Propagation Delays in Multiple Sclerosis, a Combined Tractography-Magnetoencephalography Study, J Neurosci 42 (47) (2022) 8807–8816. doi:10.1523/JNEUROSCI.0938-22.2022.

[27] P. Moretti, M. A. Muñoz, Griffiths phases and the stretching of criticality in brain networks, Nat Commun 4 (2521). doi:10.1038/ncomms3521.

[28] D. Plenz, Criticality in cortex: neuronal avalanches and coherence potentials, In: Criticality in neural systems (2014) 5–42doi:10.1002/9783527651009.ch2.

[29] O. Arviv, A. Goldstein, O. Shriki, Neuronal avalanches and time-frequency representations in stimulus-evoked activity, Sci Rep 16 (13319). doi:10.1038/s41598-019-49788-5.

[30] S. R. Miller, S. Yu, D. Plenz, The scale-invariant, temporal profile of neuronal avalanches in relation to cortical γ-oscillations, Sci Rep 9 (16403). doi:10.1038/s41598-019-52326-y.

[31] P. Sorrentino, C. Seguin, R. Rucco, M. Liparoti, E. Troisi Lopez, S. Bonavita, M. Quarantelli, G. Sorrentino, V. Jirsa, A. Zalesky, The structural connectome constrains fast brain dynamics, Elife 10. doi:10.7554/eLife.67400.

[32] S. Rombetto, C. Granata, A. Vettoliere, M. Russo, Multichannel system based on a high sensitivity superconductive sensor for magnetoencephalography, Sensors 14 (2014) 12114–12126. doi:10.3390/s140712114.

[33] D. Dellavale, F. Bonini, F. Pizzo, J. Makhalova, F. Wendling, J. M. Badier, F. Bartolomei, C. G. Bénar, Spontaneous fast-ultradian dynamics of polymorphic interictal events in drug-resistant focal epilepsy, Epilepsia 64 (2023) 2027–2043. doi:10.1111/epi.17655.

[34] V. D. Blondel, J.-L. Guillaume, R. Lambiotte, E. Lefebvre, Fast unfolding of communities in large networks, J Stat Mech 2008 (P10008). doi:10.1088/1742-5468/2008/10/P10008.

[35] M. Rubinov, O. Sporns, Weight-conserving characterization of complex functional brain networks, Neuroimage 56. doi:10.1016/j.neuroimage.2011.03.069.

[36] Shafiei, G. and Zeighami, Y. and Clark, C. A. and Coull, J. T. and Nagano-Saito, A. and Leyton, M. and Dagher, A. and Mišic, B., Dopamine Signaling Modulates the Stability and Integration of Intrinsic Brain Networks, Cereb Cortex 29 (2019) 397–409. doi:10.1093/cercor/bhy264.

[37] A. Lancichinetti, S. Fortunato, Consensus clustering in complex networks, Sci Rep 2 (336). doi:10.1038/srep00336.

[38] D. S. Bassett, M. A. Porter, N. F. Wymbs, S. T. Grafton, J. M. Carlson, P. J. Mucha, Robust detection of dynamic community structure in networks, Chaos 23 (013142). doi:10.1063/1.4790830.

[39] B. R. F., Community detection in network neuroscience, arXiv arXiv:2011.06723. doi:10.48550/arXiv.2011.06723.

[40] R. Bracewell, The Fourier Transform And Its Applications, 3rd Edition, McGraw-Hill, 2000.

[41] M. X. Cohen, Analyzing neural time series data : theory and practice, 1st Edition, MIT Press, 2014.

[42] P. Fries, A mechanism for cognitive dynamics: neuronal communication through neuronal coherence, Trends in Cognitive Sciences 9 (2005) 474–480. doi:10.1016/j.tics.2005.08.011.

[43] R. Hindriks, P. K. B. Tewarie, Dissociation between phase and power correlation networks in the human brain is driven by co-occurrent bursts, Communications Biology 6 (286). doi:10.1038/s42003-023-04648-x.

[44] A. V. Oppenheim, R. W. Schafer, J. R. Buck, Discrete-Time Signal Processing, 2nd Edition, Prentice Hall, 1998.

[45] J. G. Proakis, Digital Communications, 4th Edition, McGraw-Hill, 2000.

[46] S. Haykin, Communication Systems, 4th Edition, John Wiley & Sons, 2000.

[47] P. Berens, CircStat: A MATLAB Toolbox for Circular Statistics, Journal of Statistical Software 31 (10) (2009) 1–21. doi:10.18637/jss.v031.i10.

[48] P. Tass, M. G. Rosenblum, J. Weule, J. Kurths, A. Pikovsky, J. Volkmann, A. Schnitzler, H.-J. Freund, Detection of $n : m$ Phase Locking from Noisy Data: Application to Magnetoencephalography, Physical Review Letters 81 (0) (1998) 3291–3294. doi:10.1103/PhysRevLett.81.3291.

[49] J. P. Lachaux, E. Rodriguez, J. Martinerie, F. J. Varela, Measuring phase synchrony in brain signals, Hum Brain Mapp 8 (1999) 3194–208. doi:10.1002/(SICI)1097-0193(1999)8:4<194::AID-HBM4>3.0.CO;2-C.

Appendix A. Supplementary methods

Appendix A.1. Preservation of the Pearson's cross-correlation in the B-surrogates

Let us start by considering the circular cross-correlation $R_{xy}(t')$ between the time series $x(t)$ and $y(t)$ representing the activities of two brain regions [44, pp. 571, 746],

$$R_{xy}(t') = \sum_{t=0}^{N_s-1} x^*(t-t')_{\text{mod } N_s}\ y(t) \tag{A.1}$$

where $(x(t),\ y(t)) \in \mathbb{R}$ are finite-length discrete time series having N_s time samples satisfying $(x(t) = 0,\ y(t) = 0)\ \forall\ 0 > t > N_s - 1$, being $t \in \mathbb{Z}$ the discrete time index. By applying the Discrete Fourier Transform (DFT) $\mathfrak{F}\{.\}$ on both sides of eq. A.1 we obtain [44, pp. 575, 746],

$$\begin{aligned} S_{xy}(\omega) &= \mathfrak{F}\{R_{xy}(t')\} \\ &= \mathfrak{F}\{x(t)\}^*\ \mathfrak{F}\{y(t)\} = A_x(\omega)e^{-i\phi_x(\omega)}\ A_y(\omega)e^{i\phi_y(\omega)} \end{aligned} \tag{A.2}$$

where $A_x(\omega)$, $\phi_x(\omega)$ and $A_y(\omega)$, $\phi_y(\omega)$ are the magnitude and phase angle of the DFT spectrum corresponding to the signals $x(t)$ and $y(t)$, respectively. The computation of surrogate time series involves the addition of random phases $\theta(\omega)$ to the corresponding DFT spectra as follows,

$$\begin{aligned} S^s_{xy}(\omega) &= A_x(\omega)e^{-i(\phi_x(\omega)+\theta_x(\omega))}\ A_y(\omega)e^{i(\phi_y(\omega)+\theta_y(\omega))} \\ &= A_x(\omega)e^{-i\phi_x(\omega)}\ A_y(\omega)e^{i\phi_y(\omega)}\ e^{i(\theta_y(\omega)-\theta_x(\omega))} \end{aligned} \tag{A.3}$$

In the A.3, $S^s_{xy}(\omega)$ is the DFT of the circular cross-correlation associated with the surrogated time series $x^s(t) = \mathfrak{F}^{-1}\left\{A_x(\omega)e^{-i(\phi_x(\omega)+\theta_x(\omega))}\right\}$ and $y^s(t) = \mathfrak{F}^{-1}\left\{A_y(\omega)e^{-i(\phi_y(\omega)+\theta_y(\omega))}\right\}$, where $\mathfrak{F}^{-1}\{.\}$ stands for the inverse DFT. In the particular case of the B-surrogates we add the same random phase-shift in all the brain regions, that is, $\theta_x(\omega) = \theta_y(\omega)$ producing $e^{i(\theta_y(\omega)-\theta_x(\omega))} = 1$ in the eq. A.3. Under this condition, the eqs. A.2 and A.3 becomes equivalent which in turn implies the equivalence between the circular cross-correlations associated with the true data and the B-surrogate,

$$\begin{aligned} S_{xy}(\omega) = S^s_{xy}(\omega) \quad &\Longrightarrow \quad \mathfrak{F}\{R_{xy}(t')\} = \mathfrak{F}\left\{R^s_{xy}(t')\right\} \\ &\Longrightarrow \quad R_{xy}(t') = R^s_{xy}(t') \end{aligned}$$

Appendix A.2. Oscillatory mechanisms underlying the emergence of local above-threshold fluctuations

In this section we provide a detailed description of the mechanism underlying the emergence of local above-threshold fluctuations from the Fourier oscillatory constituents of the brain activity. Our analysis start by projecting the brain signal of interest $x(t)$ onto the Fourier basis functions using the Discrete Fourier Transform (DFT) equations [44, Chapters 8 and 10]. In doing so we are assuming that $x(t)$ satisfies certain conditions so the resulting spectral estimates exist

and are meaningful. Specifically, by considering finite-length time series constituted by N_s time samples, the existence of the DFT representation requires that $x(t)$ is bounded ($|x(t)| < M \in \mathbb{R}\ \forall\ 0 > t > N_s - 1$). Besides, the analyzed brain activity are in general nonstationary, that is, the time series $x(t)$ can be represented as a sum of sinusoidal components with time-varying amplitudes, frequencies, or phases. In this regard, we consider a small enough number of time samples N_s such that the spectral characteristics of the signal $x(t)$ can be assumed stationary during the analyzed time window. Thus, by considering $x(t) \in \mathbb{R}$ being a finite-length discrete time series having an even number of time samples N_s and $x(t) = 0\ \forall\ 0 > t > N_s - 1$, where $t \in \mathbb{Z}$ is the discrete time index. The analysis equation corresponding to the Discrete Fourier Transform (DFT) of $x(t)$ can be written as follows [44, p. 561, Eq. (8.67)],

$$X(k) = \sum_{t=0}^{N_s-1} x(t)e^{-i\omega_0 kt} \quad : \quad \omega_0 = \frac{2\pi}{N_s} \tag{A.4}$$

where $k \in \mathbb{Z}$ is the discrete frequency index, in general producing complex Fourier coefficients $X(k) \in \mathbb{C}$ and $X(k) = 0\ \forall\ 0 > k > N_s - 1$. Then, the synthesis equation associated with the inverse DFT (iDFT) is [44, p. 561, Eq. (8.68)],

$$x(t) = \frac{1}{N_s} \sum_{k=0}^{N_s-1} X(k)e^{i\omega_0 kt} \tag{A.5}$$

Taking into account that $X(k) = |X(k)|e^{i\phi(k)} \in \mathbb{C}$, the eq. A.5 can be rewritten as,

$$x(t) = \frac{1}{N_s} \sum_{k=0}^{N_s-1} |X(k)|e^{i(\omega_0 kt + \phi(k))} \tag{A.6}$$

The core of the proposed conceptualization is to note that the eq. A.6 can be expressed as a sum of (non-overlapping) pairwise adjacent spectral components as follows,

$$\begin{aligned} x(t) &= \frac{1}{N_s} \sum_{k=0}^{N_s/2-1} |X(2k)|e^{i(\omega_0 2kt + \phi(2k))} \\ &+ |X(2k+1)|e^{i(\omega_0(2k+1)t + \phi(2k+1))} \end{aligned}$$

$$x(t) = \frac{1}{N_s} \sum_{k=0}^{N_s/2-1} \left(|X(2k)|e^{i\phi(2k)} + |X(2k+1)|e^{i(\omega_0 t + \phi(2k+1))} \right) e^{i\omega_0 2kt}$$

By defining the forward phase difference as $\Delta\phi(2k) = \phi(2k+1) - \phi(2k)$, and substituting $\phi(2k+1) = \phi(2k) + \Delta\phi(2k)$ in the previous equation we have,

$$\begin{aligned} x(t) &= \frac{1}{N_s} \sum_{k=0}^{N_s/2-1} \Bigg(|X(2k)|e^{-i\left(\frac{\omega_0}{2}t + \frac{\Delta\phi(2k)}{2}\right)} \\ &+ |X(2k+1)|e^{i\left(\frac{\omega_0}{2}t + \frac{\Delta\phi(2k)}{2}\right)} \Bigg) e^{i\frac{\omega_0}{2}t} e^{i\left(\phi(2k) + \frac{\Delta\phi(2k)}{2}\right)} e^{i\omega_0 2kt} \end{aligned}$$

$$
\begin{aligned}
x(t) &= \frac{1}{N_s}\sum_{k=0}^{N_s/2-1}\Bigg(|X(2k)|e^{-i\left(\frac{\omega_0}{2}t+\frac{\Delta\phi(2k)}{2}\right)} \\
&+ |X(2k+1)|e^{i\left(\frac{\omega_0}{2}t+\frac{\Delta\phi(2k)}{2}\right)}\Bigg)e^{i\left(\frac{\omega_0}{2}(4k+1)t+\phi(2k)+\frac{\Delta\phi(2k)}{2}\right)}
\end{aligned}
$$

Then, by introducing in the previous equation the forward frequency difference $\Delta\omega = \omega_0\ (k+1) - \omega_0\ k = \omega_0$, it results,

$$
\begin{aligned}
x(t) &= \frac{1}{N_s}\sum_{k=0}^{N_s/2-1}\Bigg(|X(2k)|e^{-i\left(\frac{\Delta\omega}{2}t+\frac{\Delta\phi(2k)}{2}\right)} \\
&+ |X(2k+1)|e^{i\left(\frac{\Delta\omega}{2}t+\frac{\Delta\phi(2k)}{2}\right)}\Bigg)e^{i\left(\frac{\Delta\omega}{2}(4k+1)t+\phi(2k)+\frac{\Delta\phi(2k)}{2}\right)}
\end{aligned}
$$

Taking out $\Delta\omega/2$ as a common factor we have,

$$
\begin{aligned}
x(t) &= \frac{1}{N_s}\sum_{k=0}^{N_s/2-1}\Bigg(|X(2k)|e^{-i\frac{\Delta\omega}{2}\left(t+\frac{\Delta\phi(2k)}{\Delta\omega}\right)} \\
&+ |X(2k+1)|e^{i\frac{\Delta\omega}{2}\left(t+\frac{\Delta\phi(2k)}{\Delta\omega}\right)}\Bigg)e^{i\left(\frac{\Delta\omega}{2}(4k+1)t+\phi(2k)+\frac{\Delta\phi(2k)}{2}\right)}
\end{aligned}
$$

The rate of change of the phase with the frequency is associated with the group delay defined as $\tau(k) = -\Delta\phi(k)/\Delta\omega$. Using this definition, the previous equation can be written as,

$$
\begin{aligned}
x(t) &= \frac{1}{N_s}\sum_{k=0}^{N_s/2-1}\underbrace{\left(|X(2k)|e^{-i\frac{\Delta\omega}{2}(t-\tau(2k))}+|X(2k+1)|e^{i\frac{\Delta\omega}{2}(t-\tau(2k))}\right)}_{\text{Complex envelope (sidebands)}} \\
&\times \underbrace{e^{i\left(\frac{\Delta\omega}{2}(4k+1)t+\phi(2k)+\frac{\Delta\phi(2k)}{2}\right)}}_{\text{Complex carrier}} \qquad \text{(A.7)}
\end{aligned}
$$

It is essential to note that in eq. A.7, each (non-overlapping) pair of adjacent spectral components $X(2k), X(2k+1)$ can be interpreted as the sidebands of an amplitude modulated carrier at $(4k+1)\Delta\omega/2$. Importantly, the frequency of the carrier $(4k+1)\Delta\omega/2$ is a function of the frequency index k, that is, it depends on the particular pair of spectral components under consideration $(X(2k), X(2k+1))$. However, the frequency of the modulating component is the same for all the pair of spectral components involved in eq. A.7, i.e., it is independent of the frequency index k and only determined by the frequency resolution of the DFT as $\Delta\omega/2 = \omega_0/2$ (i.e., half the separation between the two sidebands). Another important characteristic of the representation given by the eq. A.7 is that the frequencies associated with the complex envelopes $(\Delta\omega/2)$ and with the complex carrier $((4k+1)\Delta\omega/2)$ satisfy the condition $\Delta\omega/2 \leq (4k+1)\Delta\omega/2$. In the telecom theory, a spectral profile satisfying these characteristics is known as

the complex baseband representation of a band-limited signal (e.g., amplitude modulated signal) [44, Chapter 11.4.2, p. 796; 45, Chapter 4.1, p. 152; 46, Chapter A2.4, p. 725]. Accordingly, we refer to the eq. A.7 as the inverse DFT based on the pairwise complex baseband representation of $x(t)$. In line with this, the eq. A.7 can be rewritten as a summation of amplitude modulated signals corresponding to each pair of adjacent spectral components as follows,

$$x(t) = \frac{1}{N_s} \sum_{k=0}^{N_s/2-1} x_{k+}(t) \tag{A.8}$$

$$x_{k+}(t) = \tilde{x_k}(t-\tau(k))\ e^{i\left(\frac{\Delta\omega}{2}(4k+1)t+\phi(2k)+\frac{\Delta\phi(2k)}{2}\right)} \tag{A.9}$$

$$\tilde{x_k}(t-\tau(k)) = |X(2k)|e^{-i\frac{\Delta\omega}{2}(t-\tau(2k))} + |X(2k+1)|e^{i\frac{\Delta\omega}{2}(t-\tau(2k))} \tag{A.10}$$

In the eq. A.8, $x_{k+}(t)$ is the discrete time analytic signal (a.k.a., pre-envelope) corresponding to each amplitude modulated component constituting the original signal $x(t)$, and it is defined in eq. A.9. In the eq. A.9, $\tilde{x_k}(t-\tau(k))$ is the complex envelope of each amplitude modulated component constituting the original signal $x(t)$, and it is defined in terms of the spectral components $X(k)$ in the eq. A.10. It is important to note that the alignment in time of the complex envelopes $\tilde{x_k}(t-\tau(k))$ synthesizing the original signal $x(t)$, via the eq. A.8, is determined by the group delay $\tau(k)$.

The eqs. A.7 - A.10 constitute a useful conceptualization linking the DFT and the complex baseband representation to explain the emergence of salient events from the Fourier oscillatory constituents of a band-limited signal. Due to the fact that the analysis proposed above is based on the DFT, in the case of $x(t) \in \mathbb{R}$ the result of the summation in eqs. A.7 and A.8 is guaranteed to be real valued. At the same time, this also restrict the validity of the analysis to harmonic spectral components $\omega_0\ k$ associated with the fundamental frequency $\omega_0 = 2\pi/N_s$. Now we will present the general equations valid for all the cases, that is, harmonic ($\Delta\omega(k) = \text{cte},\ \omega(k+1)/\omega(k) \in \mathbb{Q}$), non-harmonic ($\Delta\omega(k) = \text{cte},\ \omega(k+1)/\omega(k) \in \mathbb{R}\setminus\mathbb{Q}$) and non-uniformly spaced ($\Delta\omega(k) \neq \text{cte}$) Fourier oscillatory components. Let us consider a real valued signal $x(t) \in \mathbb{R}$ resulting from the linear superposition of an even number N_s of oscillatory components of arbitrary amplitude $A(k)$, frequency $\omega(k)$ and phase $\phi(k)$.

$$x(t) = \sum_{k=0}^{N_s-1} A(k)\ \cos\left(\omega(k)t + \phi(k)\right) : A(k) \in \mathbb{R} \tag{A.11}$$

Since the eq. A.11 is linear we can introduce the complex notation via the Euler's formula as follows,

$$x(t) = \mathfrak{Re}\left\{ \sum_{k=0}^{N_s-1} A(k)\ e^{i(\omega(k)t+\phi(k))} \right\} \tag{A.12}$$

In the eq. A.12, the operator $\mathfrak{Re}\{.\}$ stands for "the real part of". By following a similar procedure applied above on the eq. A.6, the eq. A.12 can be rewritten

as follows,

$$
\begin{aligned}
x(t) &= \mathfrak{Re}\Bigg\{ \sum_{k=0}^{N_s/2-1} \Bigg(A(2k)\ e^{-i\left(\frac{\Delta\omega(2k)}{2}t+\frac{\Delta\phi(2k)}{2}\right)} + A(2k+1)\ e^{i\left(\frac{\Delta\omega(2k)}{2}t+\frac{\Delta\phi(2k)}{2}\right)} \Bigg) \\
&\times\ e^{i\left(\bar{\omega}(2k)t+\bar{\phi}(2k)\right)} \Bigg\} \\
\Delta\phi(2k) &= \phi(2k+1) - \phi(2k) \\
\bar{\phi}(2k) &= \frac{\phi(2k+1)+\phi(2k)}{2} = \phi(2k) + \frac{\Delta\phi(2k)}{2} \\
\Delta\omega(2k) &= \omega(2k+1) - \omega(2k) \\
\bar{\omega}(2k) &= \frac{\omega(2k+1)+\omega(2k)}{2} = \omega(2k) + \frac{\Delta\omega(2k)}{2}
\end{aligned}
$$

In this case the group delay is defined as $\tau(k) = -\frac{\Delta\phi(k)}{\Delta\omega(k)}$, thus, the previous equation results,

$$
\begin{aligned}
x(t) &= \mathfrak{Re}\Bigg\{ \sum_{k=0}^{N_s/2-1} \underbrace{\Bigg(A(2k)\ e^{-i\frac{\Delta\omega(2k)}{2}(t-\tau(2k))} + A(2k+1)\ e^{i\frac{\Delta\omega(2k)}{2}(t-\tau(2k))} \Bigg)}_{\text{Complex envelope (sidebands)}} \\
&\times\ \underbrace{e^{i\left(\bar{\omega}(2k)t+\bar{\phi}(2k)\right)}}_{\text{Complex carrier}} \Bigg\} \qquad \text{(A.13)}
\end{aligned}
$$

The eq. A.13 is the pairwise complex baseband representation of the signal $x(t)$. Provided that the frequencies associated with the complex envelopes $(\Delta\omega(2k)/2)$ and the complex carrier $(\bar{\omega}(2k))$ satisfy the condition $\Delta\omega(2k)/2 < \bar{\omega}(2k)$, the eq. A.13 can also be written as a summation of discrete time analytic signals $x_{k+}(t)$ associated with amplitude modulated signals corresponding to each pair of adjacent oscillatory components as follows,

$$
x(t) = \mathfrak{Re}\Bigg\{ \sum_{k=0}^{N_s/2-1} x_{k+}(t) \Bigg\} \qquad \text{(A.14)}
$$

$$
x_{k+}(t) = \tilde{x_k}(t-\tau(k))\ e^{i\left(\bar{\omega}(2k)t+\bar{\phi}(2k)\right)} \qquad \text{(A.15)}
$$

$$
\begin{aligned}
\tilde{x_k}(t-\tau(k)) &= A(2k)\ e^{-i\frac{\Delta\omega(2k)}{2}(t-\tau(2k))} \\
&+ A(2k+1)\ e^{i\frac{\Delta\omega(2k)}{2}(t-\tau(2k))} \qquad \text{(A.16)}
\end{aligned}
$$

Similarly to the previous case the time alignment of the complex envelopes $\tilde{x_k}(t-\tau(k))$ synthesizing the original signal $x(t)$, via the eq. A.14, is determined by the group delay $\tau(k)$.

In what follows we will use the eq. A.13 to illustrate the role of the group delay in explaining the emergence of above-threshold fluctuations from the oscillatory constituents of the synthetic signal $x(t)$. As a first example, let us consider a spectral profile given by set of constant-amplitude $A(k) = A = 1$

oscillatory components uniformly spaced $f_s\ \Delta\omega/(2\pi) = 1.2/\sqrt{2}$ Hz and having non-harmonic frequencies $f_s\ \omega(k)/(2\pi) = 0.5 + k\ f_s\ \Delta\omega/(2\pi) \in [0.5 - 5]$ Hz, where $f_s = 1024$ Hz is the sampling rate (see Figs. A.1A and A.1F). Accordingly, the eq. A.13 becomes,

$$x(t) = A\ \mathfrak{Re}\left\{ \sum_{k=0}^{N_s/2-1} \left(e^{-i\frac{\Delta\omega}{2}(t-\tau(2k))} + e^{i\frac{\Delta\omega}{2}(t-\tau(2k))} \right) e^{i\left(\bar{\omega}(2k)t+\bar{\phi}(2k)\right)} \right\}$$

By using the Euler's formula to rearrange the modulating factor, the previous equation results,

$$\begin{aligned} x(t) &= \frac{A}{2}\ \mathfrak{Re}\left\{ \sum_{k=0}^{N_s/2-1} \cos\left(\frac{\Delta\omega}{2}\,(t-\tau(2k)) \right) e^{i\left(\bar{\omega}(2k)t+\bar{\phi}(2k)\right)} \right\} \\ &= \frac{A}{2} \sum_{k=0}^{N_s/2-1} \underbrace{\cos\left(\frac{\Delta\omega}{2}\,(t-\tau(2k)) \right)}_{\text{Modulating component}} \underbrace{\cos\left(\bar{\omega}(2k)t + \bar{\phi}(2k) \right)}_{\text{Modulated component}} \end{aligned} \quad \text{(A.17)}$$

The eq. A.17 explicitly shows that any pair of adjacent oscillatory components associated with the signal $x(t)$ can be interpreted as an amplitude modulated signal with the same modulating function $\cos\left(\frac{\Delta\omega}{2}\,(t-\tau(2k)) \right)$. The key concept here is to note that, when all the oscillatory components in eq. A.17 are added together to synthesize the signal $x(t)$ in the time domain, the group delay τ will determine the time alignment of the modulating functions associated with each pair of adjacent oscillatory components. As a consequence, in the case of all the spectral components $A(k)\ e^{i(\omega(k)t+\phi(k))}$ in eq. A.12 having constant phase produces $\Delta\phi = 0 \implies \tau = -\Delta\phi/\Delta\omega = 0$, hence, all the modulating functions $\cos\left(\frac{\Delta\omega}{2}\,(t-0) \right)$ in eq. A.17 will be aligned in time (at $t = 0$) giving rise to a sinc-like function representing the maximum amplitude excursion (i.e., a salient event) that can be elicited by the set of Fourier oscillatory components constituting the eq. A.12. In the case of all the spectral components in eq. A.12 having a phase proportional to the discrete frequency index $\phi(k) = -\tau_0\ \Delta\omega\ k \implies \Delta\phi(k) = -\tau_0\ \Delta\omega$, results in a group delay which does not dependent on the frequency $\tau(k) = -\Delta\phi(k)/\Delta\omega = \tau_0$, thus, in eq. A.12 we obtain a modulating component $\cos\left(\frac{\Delta\omega}{2}\,(t-\tau_0) \right)$. That is, all the modulating functions will again be aligned in time producing the same salient event given by the sinc-like function as in the previous case but this time centered at $t = \tau_0$ (i.e., a time-shift, see Figs. A.1A-E). On the other hand, in the case of the phases associated with the spectral components in eq. A.12 having a non-linear dependence with the discrete frequency index, e.g., $\phi(k) = -\tau_0\ \Delta\omega\ k^2 \implies \Delta\phi(k) = -\tau_0\ \Delta\omega(2k+1)$, the group delay results a function of the frequency $\tau(k) = \tau_0(2k+1)$, hence, preventing the alignment in time of the modulating functions associated with each pair of adjacent spectral

components $\cos\left(\frac{\Delta\omega}{2}\left(t-\tau(k)\right)\right)$. In this case, the signal $x(t)$ discloses sub-threshold excursions of amplitude (see Figs. A.1F-J). It is worth mentioning that in deriving the pairwise complex baseband representation of $x(t)$ given by the eqs. A.7 and A.13, we grouped the original spectral components (eqs. A.5 and A.11) in subsets of (non-overlapping) pairs adjacent in frequency. The strategy of grouping the spectral components in subsets is necessary to obtain a representation based on a sum of complex envelopes modulating the complex carriers. Representations similar to those presented in the eqs. A.7 and A.13 can be obtained by defining subsets containing more than 2 non-overlapping spectral components (not necessarily adjacent in frequency). However, our approach based on grouping adjacent spectral components in non-overlapping pairs discloses the following relevant features:

1 By defining subsets of 2 spectral components, we obtain the simplest complex envelopes characterized by a cos- or sin-like waveform shape (see the modulating component in the eq. A.17 and the colored solid lines in Figs.A.1E and A.2E).
2 By defining pairs of spectral components adjacent in frequency, we maximize the waveform shape similarity among the resulting complex envelopes. In the case of uniformly spaced spectral components ($\Delta\omega = \text{cte}$), we obtain complex envelopes having the same time period $2/\Delta\omega$ (see the colored doted lines in Figs.A.1E and A.2E).
3 By defining pairs of spectral components adjacent in frequency, we also maximize the similarity among the resulting complex carriers (see the colored solid lines in Figs.A.1E and A.2E).

Taking together, these features are of particular importance to support the link between the spectral group delay consistency (SGDC) defining the time alignment of the modulating components (complex envelopes) with the constructive interference of the modulated components (complex carriers), which in turn lead to the occurrence of salient events. As a conclusion, the results described above in connection with the eqs. A.7, A.13, show that the emergence of above-threshold fluctuations in the signal $x(t)$ is related to the consistency of the group delay $\tau(k)$ across the discrete frequency values k. That is, the occurrence of salient events is supported by a slowly varying group delay as a function of the frequency, and this hold true for harmonic, non-harmonic and also for non-uniformly spaced Fourier oscillatory constituents of the signal under analysis.

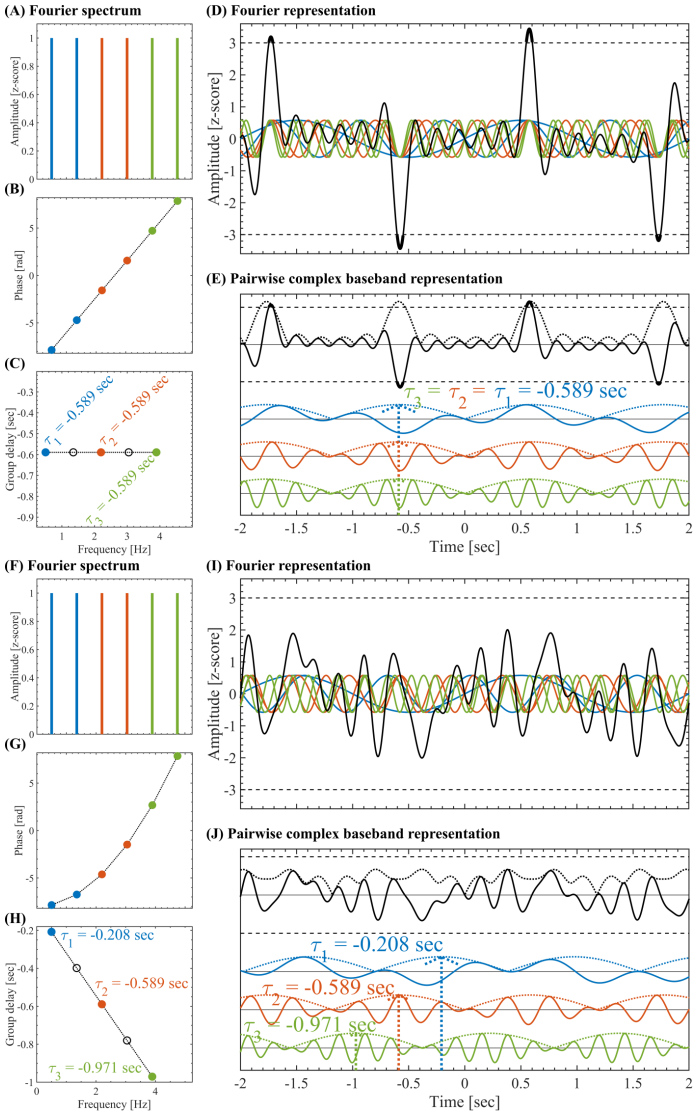

Figure A.1: Pairwise complex baseband representation for a set of oscillatory components with A_k = cte. (A) Set of constant-amplitude $A(k) = 1$ oscillatory components uniformly spaced ($f_s\ \Delta\omega/(2\pi) = 1.2/\sqrt{2}$ Hz) and having non-harmonic frequencies $f_s\ \omega(k)/(2\pi) = 0.5 + k\ f_s\ \Delta\omega/(2\pi) \in [0.5 - 5]$ Hz, where $f_s = 1024$ Hz is the sampling rate. The pairwise complex baseband representation (eq. A.13) was obtained by grouping the oscillatory components in adjacent non-overlapping pairs color-coded in blue, red and green. (B) Phases $\phi(k)$ having a linear dependence as a function of the frequency within the range $\phi(k) \in 2.5\ [-\pi, \pi]$. (C) Group delay $\tau(k)/f_s = -\Delta\phi(k)/(f_s\ \Delta\omega)$ for the pairs of adjacent oscillatory components. The color-coded filled markers correspond to the $\tau(2k)/f_s$ values, and the black empty markers correspond to $\tau(2k+1)/f_s$ values (see eq. A.13). (D) Z-scored signals. The solid color-coded lines represent the individual oscillatory components, the solid black line is the resulting signal $x(t)$, the horizontal dashed black lines indicate the threshold at $|z| = 3$. (E) Pairwise complex baseband representation. The solid color-coded lines represent the individual amplitude modulated signals (pairs of adjacent oscillatory components), the solid black line is the resulting signal $x(t)$, the color-coded and black doted lines are the corresponding amplitude envelopes. (F - J) Same as panels (A - E), this time with phases $\phi(k)$ having a quadratic dependence as a function of the frequency within the range $\phi(k) \in 2.5\ [-\pi, \pi]$ (see panel G).

The group delay is defined in terms of the rate of change of the phase with the frequency, being independent on the amplitude of the spectral components. As a consequence, the consistency of the spectral group delay as a mechanism supporting the emergence of salient events is also valid for spectral profiles other than the constant-amplitude spectrum shown in the Fig. A.1. The Fig. A.2 shows the results for a spectral profile given by a set of (uniformly spaced) non-harmonic oscillatory components with amplitudes $A(k) \propto 1/\sqrt{k}$, that is, the power of the spectral components $A^2(k)$ is proportional to $1/k$ (see Figs. A.2A and A.2F). Figs. A.2A-E show the case in which the phases $\phi(k)$ of the spectral components $A(k)\ e^{i(\omega(k)t+\phi(k))}$ in eq. A.12 are randomly distributed in a very small range around zero ($\phi(k) \in [-\pi/10, \pi/10]$). Under this condition, the pairwise complex baseband representation (eq. A.13) shown in the Fig. A.2E is constituted by amplitude modulated signals highly aligned in time. As a consequence, prominent salient events can be distinguished in the resulting signal (see solid black line in panels D and E of Fig. A.2). On the other hand, Figs. A.2A-E show the case in which the phase values $\phi(k)$ are randomly distributed in a wider range $\phi(k) \in [-\pi, \pi]$. Under this condition, the pairwise complex baseband representation (eq. A.13) shown in the Fig. A.2J is constituted by amplitude modulated signals non-aligned in time. As a consequence, the resulting signal $x(t)$ only discloses sub-threshold excursions of amplitude (see solid black line in panels I and J of Fig. A.2).

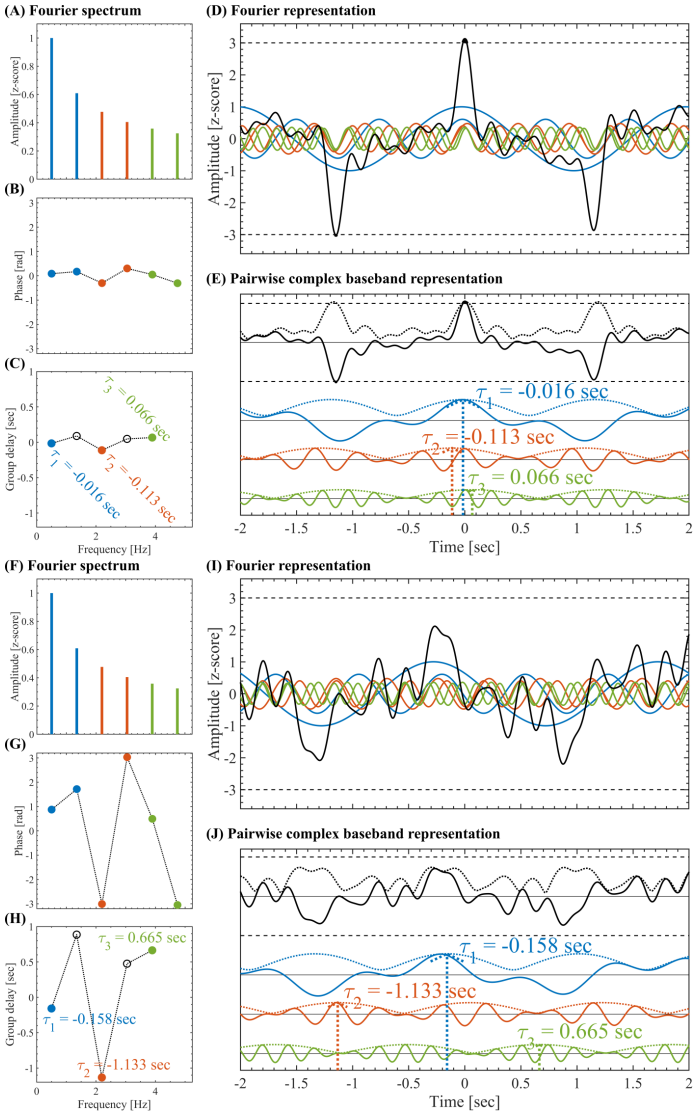

Figure A.2: Pairwise complex baseband representation for a set of oscillatory components with $A(k) \propto 1/\sqrt{k}$. (A) Set of non-constant amplitude $A(k) \propto 1/\sqrt{k}$ oscillatory components uniformly spaced ($f_s\ \Delta\omega/(2\pi) = 1.2/\sqrt{2}$ Hz) and having non-harmonic frequencies $f_s\ \omega(k)/(2\pi) = 0.5 + k\ f_s\ \Delta\omega/(2\pi) \in [0.5 - 5]$ Hz, where $f_s = 1024$ Hz is the sampling rate. The pairwise complex baseband representation (eq. A.13) was obtained by grouping the oscillatory components in adjacent non-overlapping pairs color-coded in blue, red and green. (B) Phases $\phi(k)$ randomly distributed within a very small range around zero ($\phi(k) \in [-\pi/10, \pi/10]$). (C) Group delay $\tau(k)/f_s = -\Delta\phi(k)/(f_s\ \Delta\omega)$ for the pairs of adjacent oscillatory components. The color-coded filled markers correspond to the $\tau(2k)/f_s$ values, and the black empty markers correspond to $\tau(2k+1)/f_s$ values (see eq. A.13). (D) Z-scored signals. The solid color-coded lines represent the individual oscillatory components, the solid black line is the resulting signal $x(t)$, the horizontal dashed black lines indicate the threshold at $|z| = 3$. (E) Pairwise complex baseband representation. The solid color-coded lines represent the individual amplitude modulated signals (pairs of adjacent oscillatory components), the solid black line is the resulting signal $x(t)$, the color-coded and black doted lines are the corresponding amplitude envelopes. (F - J) Same as panels (A - E), this time the phases $\phi(k)$ are randomly distributed within the range $\phi(k) \in [-\pi, \pi]$ (see panel G).

In summary, the analytical arguments presented above, condensed in the eqs. A.7 - A.10 and A.13 - A.16, allowed us to identify the consistency of the group delay across the spectral components as a mechanism explaining the emergence of above-threshold fluctuations from the Fourier oscillatory constituents of the activity associated with a single brain region. In the next section we describe the signal processing tools proposed to quantify the SGDC in empirical data.

Appendix A.3. Measures to assess the spectral group delay consistency

The analytical arguments presented in the Appendix A.2 have profound consequences regarding the interpretation of the experimental results in connection with the emergence of salient events from narrowband oscillations and broadband $1/f$ activity. Specifically, the pairwise complex baseband representation of band-limited signals (eqs. A.7 - A.10 and A.13 - A.16), explicitly shows that the mechanism underlying the emergence of above-threshold fluctuations in a signal $x(t)$ can be understood in terms of the consistency of the group delay across the Fourier oscillatory constituents of the signal (see the complex envelopes $\tilde{x_k}(t-\tau(k))$ in eqs. A.10 and A.16). By considering a multi-regional approach, the pairwise complex baseband representation can be applied on the activity $x_r(t)$ of each brain region r, to obtain complex envelopes of the form $\tilde{x}_{r,k}(t-\tau_r(k))$. Here we recall that $\tilde{x}_{r,k}(t-\tau_r(k))$ determine the envelopes of the individual amplitude modulated signals constituting the signal $x_r(t)$ (see the solid and doted color-coded curves in the Figs. A.1E,J and A.2E,J). Hence, the consistency of the spectral group delay $\tau_r(k)$ determines the synchronization of the complex envelopes $\tilde{x}_{r,k}(t-\tau_r(k))$ across both frequency values $\omega(k)$ and brain regions r. In what follows we describe the proposed measures designed to quantify the spectral group delay consistency (SGDC) in experimental data across either frequency values and/or brain regions. In order to simplify the notation, in the rest of this section we will use ω instead of the discrete frequency index k, implicitly assuming that $\omega = \omega(k)$. In the most general case, the spectral group delay can be estimated as $\tau_r(\omega) = -\Delta\phi_r(\omega)/\Delta\omega(\omega)$, where $\Delta\phi_r(\omega)$ and $\Delta\omega(\omega)$ are the incremental phase and incremental frequency between adjacent spectral components associated with the activity $x_r(t)$ of the brain region r, respectively. Let us consider first the particular case of $\Delta\omega(\omega) = \Delta\omega = \text{cte.}$, in which the group delay results $\tau_r(\omega) \propto -\Delta\phi_r(\omega)$. Therefore, the SGDC can be simply assessed via the Euler's transform of the incremental phase as follows,

$$SGDC(r) = \frac{1}{N}\sum_{\omega} e^{-i\Delta\phi_r(\omega)} : \Delta\omega = \text{cte. across } r \tag{A.18}$$

$$SGDC(\omega) = \frac{1}{N}\sum_{r} e^{-i\Delta\phi_r(\omega)} : \Delta\omega = \text{cte. across } \omega \tag{A.19}$$

The modulus of eqs. A.18 and A.19 satisfies,

$$|SGDC| = \left|\frac{1}{N}\sum e^{-i\Delta\phi_r(\omega)}\right| = R = (1-S) \in [0,1] \tag{A.20}$$

In the eqs. A.18, A.19 and A.20, N is the number of either frequency values or brain regions as appropriate, R is the resultant vector length and S is the circular variance [47]. The eq. A.20 explicitly shows that the SGDC is assessed as one minus the circular variance of the incremental phase. The definition of the SGDC measures given in the eqs. A.18, A.19 and A.20 should not be confused with the traditional measure for quantifying coherence known as Phase Locking Value (PLV) [48, 49]. Specifically, the SGDC measures as defined in the eqs. A.18, A.19 and A.20 assess the consistency of the incremental phase $\Delta\phi_r(\omega)$ across the frequency values ω. In contrast, the PLV assesses the consistency of phase difference across the time samples, where the phase difference is computed between two phase time series corresponding to two specific frequency bands in the same or different brain regions [48, 49]. As stated in the eq. A.18, the $SGDC(r)$ is a bounded measure in the range $[0, 1]$ and quantifies how much the group delay varies across the spectral components conforming the activity of interest $x_r(t)$. On the one hand, constant group delay values $\tau_r(\omega) \propto -\Delta\phi_r(\omega)$ across the spectral components produce $|SGDC(r)| \approx 1$ indicating a high SGDC, which is associated with high burstiness of the signal $x_r(t)$ (see Figs. A.1A-E and A.2A-E). On the other hand, in the case of group delay values varying randomly (or non-linearly) across the spectral components produces $|SGDC(r)| \approx 0$ indicating low SGDC associated with low burstiness of the signal $x_r(t)$ (see Figs. A.1F-J and A.2F-J). Similarly, the $SGDC(\omega)$ defined in the eq. A.19 is a bounded measure in the range $[0, 1]$ and quantifies how much the spectral group delay at a given frequency ω, varies across the brain regions r. On the one hand, constant group delay values $\tau_r(\omega) \propto -\Delta\phi_r(\omega)$ across the brain regions produce $|SGDC(\omega)| \approx 1$ indicating a high group delay consistency, which is associated with high cross-regional synchronization of the bursts at a given frequency ω. On the other hand, in the case of group delay values varying randomly (or non-linearly) across the brain regions produces $|SGDC(\omega)| \approx 0$ indicating low group delay consistency associated with low cross-regional synchronization of the bursts at a given frequency ω. Now we will consider the more general case in which $\Delta\omega(k) \neq$ cte. In line with the previous analysis, the SGDC measures can be defined in terms of the linear variance of the group delay $Var(\tau)$ as follows,

$$SGDC = 1 - \frac{\mathrm{Var}(\tau)}{\max\{\mathrm{Var}(\tau)\}} \in [0, 1] \tag{A.21}$$

$$\mathrm{Var}(\tau) = \frac{1}{N} \sum (\tau - \langle\tau\rangle)^2 \tag{A.22}$$

In the eq. A.22, the mean group delay value $\langle\tau\rangle$ and the the sum associated with the linear variance $\mathrm{Var}(\tau)$ are computed across the N frequency values ω or brain regions r in which case the eq. A.21 produces $SGDC(r)$ or $SGDC(\omega)$, respectively. Importantly, the eqs. A.18, A.19 and A.21 constitute an specialized framework to quantify the emergence of large-scale bursts (i.e., brain avalanches) from the brain activity. That is, the $SGDC(r)$ measure assesses the emergence of local above-threshold fluctuations from the spectral components constituting the activity of a single brain region, whereas the $SGDC(\omega)$ measure quantifies

the synchronization of the above-threshold bursts across brain regions. In line with this, we introduce the pairwise spectral group delay consistency (pSGDC) to quantify the burstiness and cross-regional bursts synchronization in a single measure. In the case of $\Delta\omega(\omega) = \Delta\omega = \text{cte.}$, the pSGDC is defined as follows,

$$\begin{aligned} &pSGDC(r_1, r_2) = \\ &\underbrace{\left(\frac{SGDC(r_1) + SGDC(r_2)}{2}\right)}_{\text{Mean pairwise burstiness}} \underbrace{\frac{1}{N}\sum_{\omega} e^{-i(\Delta\phi_1(\omega)-\Delta\phi_2(\omega))}}_{\text{Correlation of burstiness across } \omega} \\ &: \Delta\omega = \text{cte. across } r \end{aligned} \tag{A.23}$$

In the eq. A.23, the quantities $SGDC(r_1)$ and $SGDC(r_2)$ are computed using the eq. A.18. In the case of $\Delta\omega(\omega) \neq \text{cte}$ the pSGDC is defined as follows,

$$\begin{aligned} &pSGDC(r_1, r_2) = \\ &\underbrace{\left(\frac{SGDC(r_1) + SGDC(r_2)}{2}\right)}_{\text{Mean pairwise burstiness}} \underbrace{\frac{\text{Cov}(\tau_1(\omega), \tau_2(\omega))}{\text{Var}(\tau_1(\omega))\ \text{Var}(\tau_2(\omega))}}_{\text{Correlation of burstiness across } \omega} \\ &\text{Cov}(\tau_1(\omega), \tau_2(\omega)) = \frac{1}{N}\sum_{\omega} \left(\tau_1(\omega) - \langle\tau_1(\omega)\rangle\right)\left(\tau_2(\omega) - \langle\tau_2(\omega)\rangle\right) \end{aligned} \tag{A.24}$$

In the eq. A.24, the quantities $SGDC(r_1)$ and $SGDC(r_2)$ are computed using the eqs. A.21 and A.22. Besides, the quantities $\text{Var}(\tau_1(\omega))$ and $\text{Var}(\tau_2(\omega))$ are computed using the eq. A.22. In both cases the sum associated with the eq. A.22 is computed over the frequency values ω. The eqs. A.23 and A.24 show that the $pSGDC(r_1, r_2)$ is a linear measure conformed by a factor quantifying the cross-regional correlation between the group delays across the frequency values, weighted by a coefficient quantifying the burstiness of the two involved brain regions (r_1, r_2). Importantly, we found that the pSGDC performs similarly to the cokurtosis (fourth standardized cross central moment) [43] in reproducing the observed avalanche topographies and co-activation patterns (see Fig. 6 in Section 3.6 of the main text). This is particularly interesting taking into account that these two non-time-resolved measures (i.e., computed on the whole time series) effectively reproduce the avalanche topographies through two different approaches. That is, the cokurtosis is a non-linear time-domain measure, whereas the pSGDC is a linear measure entirely based on the frequency-domain. Moreover, the pSGDC and cokurtosis disclose a better performance to reproduce the observed avalanche topographies and co-activation patterns when compared to the kurtosis (scaled version of the fourth central moment) and the Pearson's linear correlation (see discussion in Section 3.6 of the main text). These results are consistent with the fact that kurtosis measures the presence of outliers (tails of the distribution of amplitude values) and the Pearson's correlation coefficient the linear correlations between the two time series. On the other hand, pSGDC and cokurtosis measures quantify these two features simultaneously. In this work the kurtosis (K) and the cokurtosis (CK) were assessed via the following

expressions,

$$
\begin{aligned}
K(r) &= \frac{(N_s-1)}{(N_s-2)(N_s-3)}\big((N_s+1)k(r)-3(N_s-1)\big) \qquad \text{(A.25)}\\
k(r) &= \frac{\mu_{r,4}}{\sigma_r^4}\\
\mu_{r,4} &= \frac{1}{N_s}\sum_t \big(x_r-\langle x_r\rangle\big)^4\\
\sigma_r^4 &= \left(\frac{1}{N_s}\sum_t \big(x_r-\langle x_r\rangle\big)^2\right)^2
\end{aligned}
$$

$$
\begin{aligned}
CK(r_1,r_2) &= \frac{ck(r_1,r_2)}{\sigma_1^2\sigma_2^2} \qquad \text{(A.26)}\\
ck(r_1,r_2) &= \frac{1}{N_s}\sum_t \big(x_1-\langle x_1\rangle\big)^2\big(x_2-\langle x_2\rangle\big)^2\\
\sigma_r^2 &= \frac{1}{N_s}\sum_t \big(x_r-\langle x_r\rangle\big)^2
\end{aligned}
$$

In the eqs. A.25 and A.26, N_s is the number of time samples and $\langle . \rangle$ stands for mean value across the time samples.

In the rest of this section, we present illustrative examples using the eqs. A.18 and A.19 on synthetic multi-channel bursts emerging from narrowband oscillatory activity. Fig. A.3 shows the $|SGDC(r)|$ computed using the eq. A.18 for three time series synthesized using the Eq. A.11. In each channel, the signal was synthesized by the linear superposition of 10 sinusoidal tones with uniformly spaced frequencies ($\Delta\omega =$ cte.) in the range $f_s\ \omega/(2\pi) \in [0.5-3]$ Hz. In channels 1 and 2, the phase of the tones were set as a quadratic function of the frequency within the range $\phi_1(\omega) \propto 2\pi\omega^2 \in [-2\pi, 2\pi]$ and $\phi_2(\omega) \propto \pi\omega^2 \in [-\pi, \pi]$, respectively. In channel 3, the phase of the tones were set as a linear function of the frequency within the range $\phi_3(\omega) \propto \pi\omega \in [-\pi, \pi]$. Fig. A.3B shows that the higher the burstiness (i.e., amplitude of the transient fluctuations) disclosed by the resulting signal (see solid black line in the Fig. A.3A), the higher the $|SGDC(r)|$ value. The channel 3, corresponding to the tones having a linear phase dependence with the frequency, discloses the maximum $|SGDC(r)| \approx 1$.

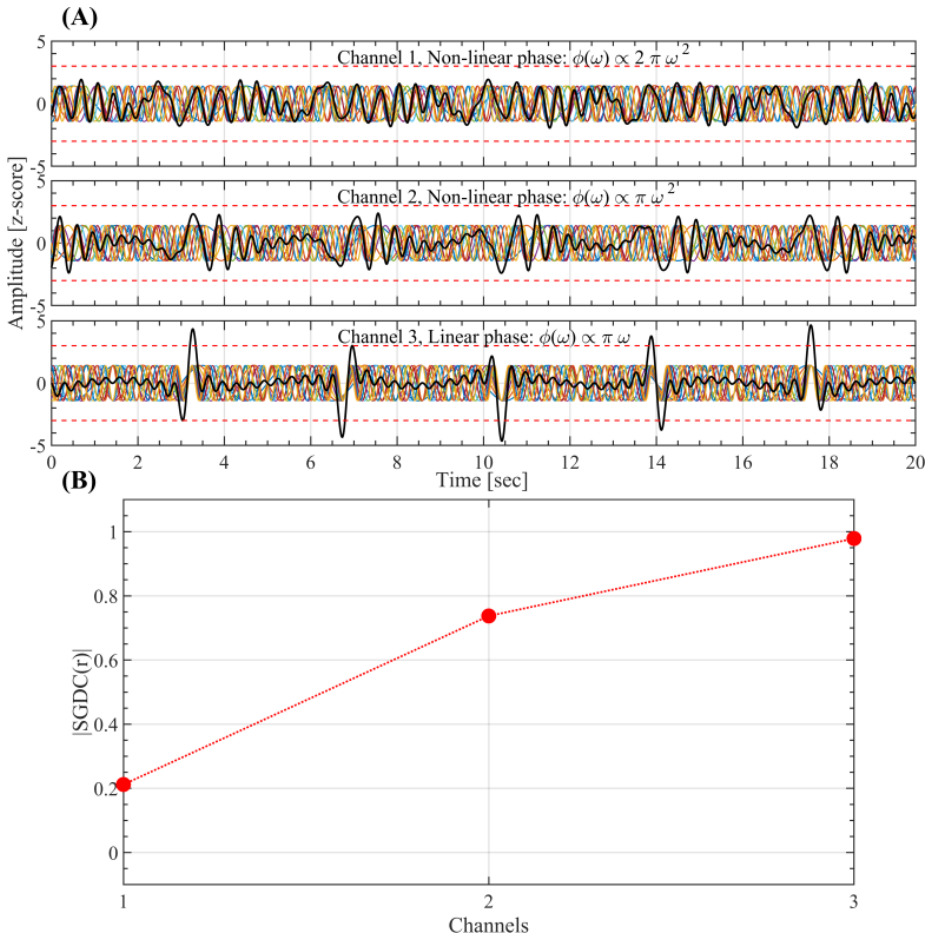

Figure A.3: $SGDC(r)$ computed using the eq. A.18 on a multi-channel configuration. (A) Three time series $x_r(t)$ (black solid lines) synthesized using the Eq. A.11. In each channel, the signal $x_r(t)$ was synthesized by the linear superposition of 10 sinusoidal tones (colored solid lines) with unitary amplitude and uniformly spaced frequencies ($f_s\ \Delta\omega/(2\pi) = 0.278$ Hz) within the range $f_s\ \omega(k)/(2\pi) = 0.5 + k\ f_s\ \Delta\omega/(2\pi) \in [0.5 - 3]$ Hz. In the channels 1 and 2, the phase of the tones were set as a quadratic function of the frequency within the range $\phi_1(\omega) \propto 2\pi\omega^2 \in [-2\pi, 2\pi]$ and $\phi_2(\omega) \propto \pi\omega^2 \in [-\pi, \pi]$, respectively. In the channel 3, the phase of the tones were set as a linear function of the frequency within the range $\phi_3(\omega) \propto \pi\omega \in [-\pi, \pi]$. (B) Modulus of the $SGDC(r)$ for each channel. Note that the higher the burstiness (i.e., amplitude of the transient fluctuations) disclosed by the resulting signal (see solid black line in the panel A), the higher the $|SGDC(r)|$ value. As expected, the channel 3 corresponding to the tones having a linear phase dependence with the frequency discloses the maximum $|SGDC(r)| \approx 1$.

Figs. A.4 and A.5 show the $SGDC(\omega)$ computed using the eq. A.19 compared against the Phase Locking Value (PLV) assessed using the following ex-

pression [48, 49],

$$PLV = \frac{1}{N} \sum_t e^{i(n\psi(t) - m\theta(t))} \tag{A.27}$$

In eq. A.27, $\psi(t)$ and $\theta(t)$ are the phase time series of interest and the integers $n, m \in \mathbb{N}$ are required to allow the comparison of phase time series pertaining to different frequency bands. Of note, the $SGDC(\omega)$ quantifies, at each frequency value, the bursts synchronization across the brain regions (channels), whereas the PLV quantifies either local or cross-regional phase coherence between two frequency bands and it is not related to the signal burstiness, i.e., the PLV is not sensitive to the emergence of above-threshold fluctuations neither to the cross-regional synchronization of salient events. Fig. A.4A shows three channels in which the resulting time series (solid black line) have been synthesized as the linear superposition of 10 sinusoidal tones with uniformly spaced frequencies ($\Delta\omega$ = cte.) in the range $f_s\ \omega/(2\pi) \in [0.5 - 3]$ Hz (see Eq. A.11). In each channel, the phase of all the oscillatory components was set to zero ($\phi_r(\omega) = 0\ \forall\ \omega$). The local and cross-regional effects of this setup can be summarized as follows,

- In each channel (local effect), we obtain the maximum group delay consistency across frequency values explaining the emergence of above-threshold fluctuations. That is, $\phi_r(\omega) = 0 \implies \Delta\phi_r(\omega) = 0 \implies \tau_r(\omega) = -\Delta\phi_r/\Delta\omega = 0 = \text{cte} \implies SGDC(r) = 1 : r = 1, 2, 3$ (data not shown).

- At each frequency, we obtain the maximum group delay consistency across channels (cross-regional effect) explaining the synchronization of the salient events across the channels. That is, $\phi_r(\omega) = 0 \implies \Delta\phi_r(\omega) = 0 \implies \tau_r(\omega) = -\Delta\phi_r/\Delta\omega = 0 = \text{cte} \implies SGDC(\omega) = 1\ \forall\ \omega$. The resulting $|SGDC(\omega)|$ is shown in Fig. A.4B.

- At each frequency, we obtain the maximum phase coherence across channels (cross-regional effect). That is, $\psi_{r,\omega}(t) - \theta_{r',\omega}(t) = 0 \implies |PLV| = 1\ \forall\ \omega$, where the phase time series $\psi_{r,\omega}(t)$ and $\theta_{r',\omega}(t)$ were extracted from different channels ($(r, r') \in \{1, 2, 3\} : r \neq r'$) and evaluated at the same frequency ω. In other words, $\psi_{r,\omega}(t)$ and $\theta_{r',\omega}(t)$ are the phase time series associated with two tones homologous in frequency and pertaining to different channels. The resulting $|PLV|$ is shown in the Fig. A.4B.

Fig. A.4C shows three time series constituted by the same 10 tones used in Fig. A.4A, with the difference that in this case the phase of the tones were set as $\phi_1(\omega) = 0$, $\phi_2(\omega) \propto -3\pi\omega$ and $\phi_3(\omega) \propto +3\pi\omega$ for the channel 1, 2 and 3, respectively. The linear phase dependence with the frequency associated with the channels 2 and 3 produces a time-shift in the resulting signals. As a consequence, in this multi-channel configuration the resulting above-threshold fluctuations are not synchronized across channels (see the solid black lines in the Fig. A.4C). In this case, the SGDC and PLV measures result,

- In each channel (local effect), we obtain the maximum group delay consistency across frequency values explaining the emergence of above-threshold

fluctuations. That is, $\Delta\phi_r(\omega) = \text{cte.} \implies \tau_r(\omega) = -\Delta\phi_r/\Delta\omega = \text{cte} \implies SGDC(r) = 1 : r = 1, 2, 3$. Note that this result is similar to what we obtained for a constant group delay (i.e., not a function of the frequency) associated with the channel 3 shown in Fig. A.3.

- At each frequency, we obtain a low group delay consistency across channels (cross-regional effect) explaining the lack synchronization of the salient events across the channels. That is, $\Delta\phi_1(\omega) = 0, \Delta\phi_2(\omega) < 0, \Delta\phi_3(\omega) > 0 \implies \tau_1(\omega) = 0, \tau_2(\omega) > 0, \tau_3(\omega) < 0 \implies SGDC(\omega) \approx 0 \; \forall \; \omega$. The resulting $|SGDC(\omega)|$ is shown in the Fig. A.4D.

- At each frequency, we obtain the maximum phase coherence across channels (cross-regional effect). That is, $\psi_{r,\omega}(t) - \theta_{r',\omega}(t) = \text{cte.} \implies |PLV| = 1 \; \forall \; \omega$, where the phase time series $\psi_{r,\omega}(t)$ and $\theta_{r',\omega}(t)$ were extracted from different channels ($(r, r') \in \{1, 2, 3\} : r \neq r'$) and evaluated at the same frequency ω. In other words, $\psi_{r,\omega}(t)$ and $\theta_{r',\omega}(t)$ are the phase time series associated with two tones homologous in frequency and pertaining to different channels. The resulting $|PLV|$ is shown in the Fig. A.4D.

It is essential to note that, the $SGDC(\omega)$ measure is highly sensitive to the cross-regional synchronization of the salient events, whereas the PLV measure is completely blind to this effect (compare Figs. A.4B and A.4D).

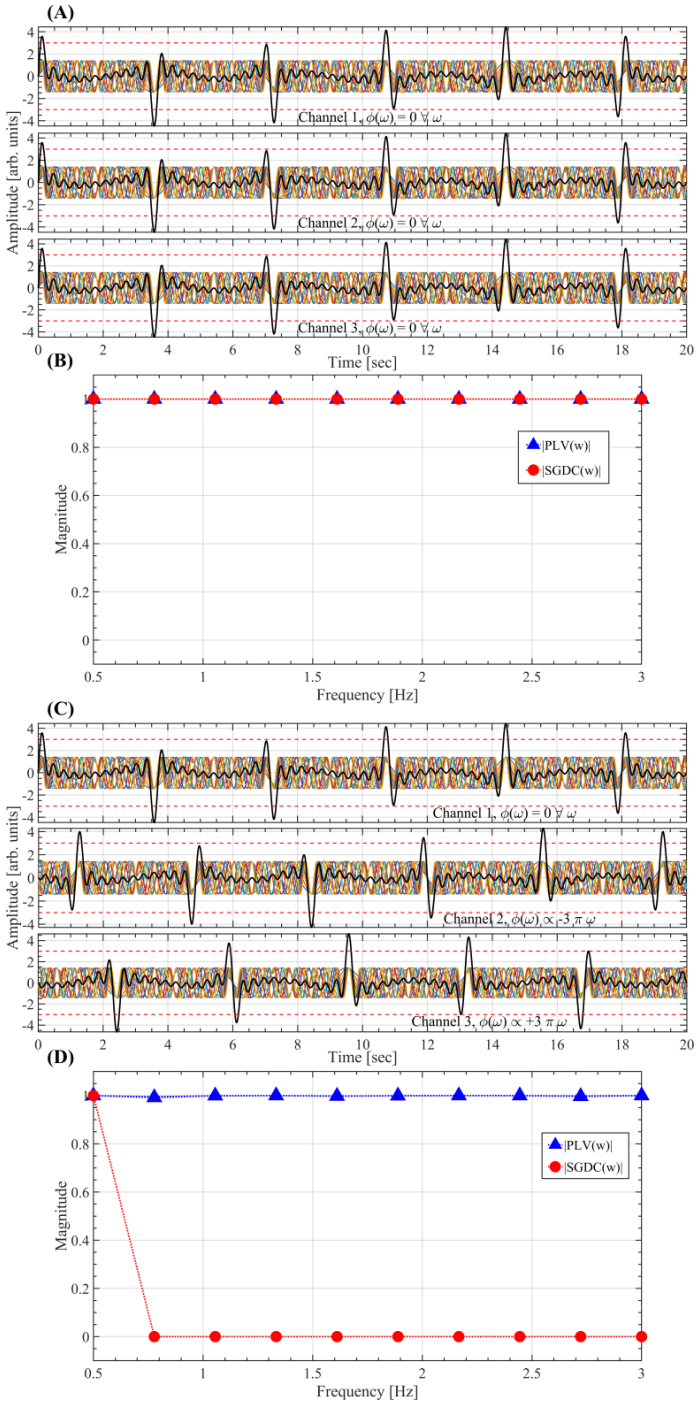

Figure A.4: $SGDC(\omega)$ computed using the eq. A.19 on a multi-channel configuration. (A) Three time series $x_r(t)$ (black solid lines) synthesized using the Eq. A.11. In each channel, the signal $x_r(t)$ was synthesized by the linear superposition of 10 sinusoidal tones (colored solid lines) with unitary amplitude and uniformly spaced frequencies ($f_s\ \Delta\omega/(2\pi) = 0.278$ Hz) within the range $f_s\ \omega(k)/(2\pi) = 0.5 + k\ f_s\ \Delta\omega/(2\pi) \in [0.5 - 3]$ Hz. In each channel, the phase of all the oscillatory components was set to zero ($\phi_r(\omega) = 0\ \forall\ \omega$). (B) $SGDC(\omega)$ and PLV measures computed using the eqs. A.19 and A.27, respectively, for the multi-channel configuration shown in panel A. (C) Same as in A, but in this case the phase of the tones were set as $\phi_1(\omega) = 0$, $\phi_2(\omega) \propto -3\pi\omega$ and $\phi_3(\omega) \propto +3\pi\omega$ for the channel 1, 2 and 3, respectively. (D) Same as in B for the multi-channel configuration shown in panel C.

Fig. A.5A shows three time series constituted by the same 10 tones used in Figs. A.4A and A.4C with the difference that in this case the phase of the tones were set as follows,

$$\begin{aligned}
\phi_1(\omega) &= 0 \ \forall \ \omega \ \text{(LF+HF)} \\
\phi_2(\omega) &\propto \begin{cases} 0, & \forall \ 0.5\text{Hz} \leq f_s \ \omega/(2\pi) \leq 1.5\text{Hz (LF)} \\ -3\pi\omega, & \forall \ 1.5\text{Hz} \leq f_s \ \omega/(2\pi) \leq 3\text{Hz (HF)} \end{cases} \\
\phi_3(\omega) &\propto \begin{cases} 0, & \forall \ 0.5\text{Hz} \leq f_s \ \omega/(2\pi) \leq 1.5\text{Hz (LF)} \\ +3\pi\omega, & \forall \ 0.5\text{Hz} \leq f_s \ \omega/(2\pi) \leq 1.5\text{Hz (HF)} \end{cases}
\end{aligned} \tag{A.28}$$

This phase configuration produce LF transient fluctuations co-occurring across the channels, while the resulting HF transient fluctuations are not synchronized across the channels (see Fig. A.5A). Importantly, the $SGDC(\omega)$ effectively discriminate the cross-regional synchronization of the transient fluctuations across the frequency values, whereas the PLV measure is again completely blind to this effect (see Fig. A.5B). Fig. A.5C shows three time series constituted by the same 10 tones used in Fig. A.5A (see Eq. A.11) with the difference that in this case the phase of the tones were set as follows,

$$\begin{aligned}
\phi_1(\omega) &= 0 \ \forall \ \omega \ \text{(LF+HF)} \\
\phi_2(\omega) &\propto \begin{cases} -3\pi\omega, & \forall \ 0.5\text{Hz} \leq f_s \ \omega/(2\pi) \leq 1.5\text{Hz (LF)} \\ 0, & \forall \ 1.5\text{Hz} \leq f_s \ \omega/(2\pi) \leq 3\text{Hz (HF)} \end{cases} \\
\phi_3(\omega) &\propto \begin{cases} +3\pi\omega, & \forall \ 0.5\text{Hz} \leq f_s \ \omega/(2\pi) \leq 1.5\text{Hz (LF)} \\ 0, & \forall \ 0.5\text{Hz} \leq f_s \ \omega/(2\pi) \leq 1.5\text{Hz (HF)} \end{cases}
\end{aligned} \tag{A.29}$$

Similarly to the previous case, the $SGDC(\omega)$ effectively discriminate the cross-regional synchronization of the transient fluctuations across the frequency values, whereas the PLV measure is again completely blind to this effect (see Fig. A.5D). It is worth mentioning that $\Delta\phi_r(\omega)$ in the eq. A.19 is the incremental phase between adjacent spectral components associated with the activity $x_r(t)$ of the brain region r. Thus, for N spectral components we obtain $N-1$ incremental phase values $\Delta\phi_r(\omega)$. As a convention, we add an extra value $\Delta\phi_r(\omega) = 0$ as the first element (i.e., lowest frequency) of the list of incremental phase values. Hence, for N spectral components the eqs. A.18 and A.19 produce N values of SGDC. In particular, the first value (i.e., lowest frequency) of $SGDC(\omega)$, associated with the artificially added $\Delta\phi_r(\omega) = 0$, is always equal to 1 (this becomes evident in the Figs. A.4D and A.5D).

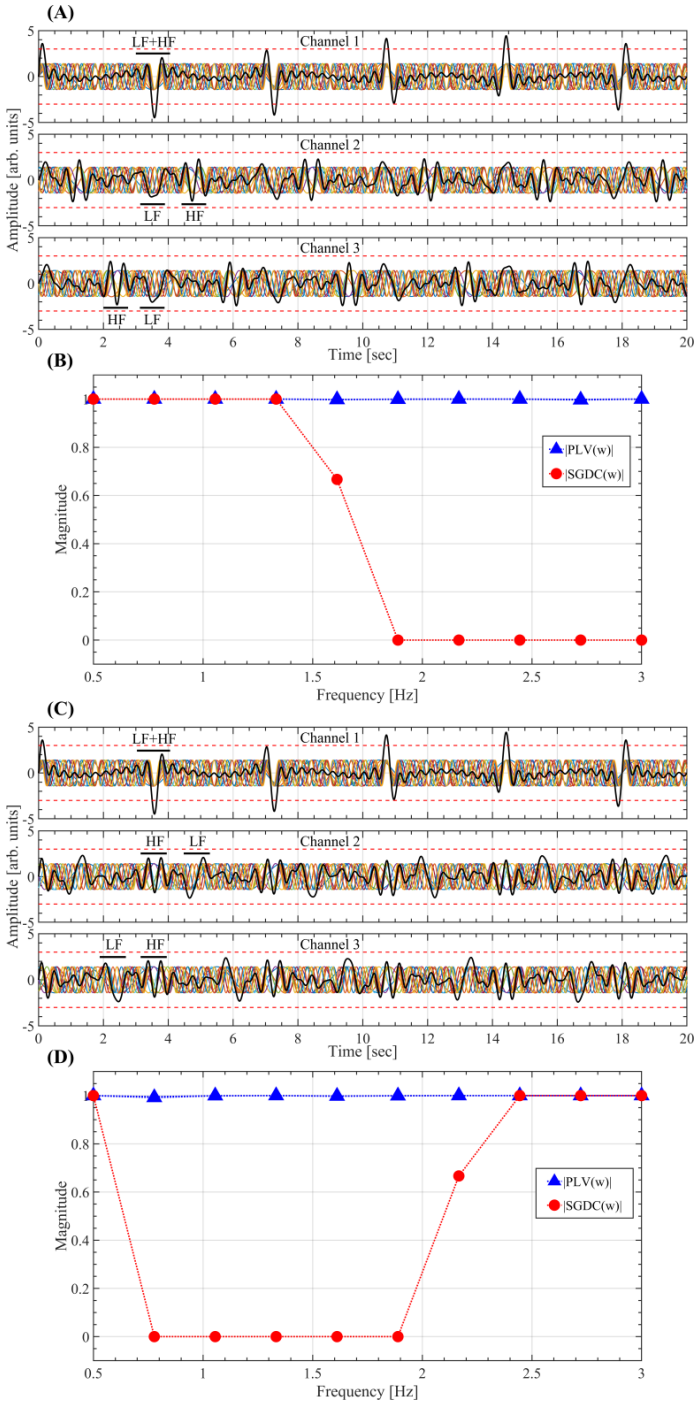

Figure A.5: $SGDC(\omega)$ computed using the eq. A.19 on a multi-channel configuration. (A) Three time series $x_r(t)$ (black solid lines) synthesized using the Eq. A.11. In each channel, the signal $x_r(t)$ was synthesized by the linear superposition of 10 sinusoidal tones (colored solid lines) with unitary amplitude and uniformly spaced frequencies ($f_s\ \Delta\omega/(2\pi) = 0.278$ Hz) within the range $f_s\ \omega(k)/(2\pi) = 0.5 + k\ 20\ \Delta\omega/(2\pi) \in [0.5 - 3]$ Hz. In each channel, the phases of the oscillatory components were configured as stated in the set of eqs. A.28. (B) $SGDC(\omega)$ and PLV measures computed using the eqs. A.19 and A.27, respectively, for the multi-channel configuration shown in panel A. (C) Same as in A, but in this case the phase of the tones were configured as stated in the set of eqs. A.29. (D) Same as in B for the multi-channel configuration shown in panel C.

Appendix A.4. Spectral group delay consistency in the surrogate data

Here we analytically show that, on the one hand, A-surrogates significantly reduce the spectral group delay consistency (SGDC) across both frequency values ($SGDC(r)$) and brain regions ($SGDC(\omega)$). On the other hand, B-surrogates significantly reduce the SGDC across frequency values ($SGDC(r)$), while preserving the SGDC across brain regions ($SGDC(\omega)$).
We start by recalling the definition of $SGDC(r)$ and $SGDC(\omega)$ for a multi-regional time series $x_r(t)$,

$$\begin{aligned}
\mathfrak{F}\{x_r(t)\} &= X_r(\omega) = A_r(\omega)e^{i\phi_r(\omega)} \\
\Delta\phi_r(\omega) &= \phi_r(\omega+\Delta\omega) - \phi_r(\omega) \\
SGDC(r) &= \frac{1}{N}\sum_{\omega} e^{-i\Delta\phi_r(\omega)} : \Delta\omega = \text{cte. across } r \qquad \text{(A.30)} \\
SGDC(\omega) &= \frac{1}{N}\sum_{r} e^{-i\Delta\phi_r(\omega)} : \Delta\omega = \text{cte. across } \omega \qquad \text{(A.31)}
\end{aligned}$$

where $A_r(\omega)$ and $\phi_r(\omega)$ are the amplitude and phase Fourier spectra, respectively. In eqs. A.30 and A.31, N is the number of either frequency values or brain regions, respectively, and $\Delta\phi_r(\omega)$ is the incremental phase computed across the spectral components of the DFT spectrum $X_r(\omega)$ associated with the signals $x_r(t)$. In the case of the surrogate multi-regional time series $x_r^s(t)$, obtained by phase randomization of the original time series in the frequency domain, we have,

$$\begin{aligned}
\mathfrak{F}\{x_r^s(t)\} &= X_r^s(\omega) = A_r(\omega)e^{i(\phi_r(\omega)+\theta_r(\omega))} \\
SGDC^s(r) &= \frac{1}{N}\sum_{\omega} e^{-i(\Delta\phi_r(\omega)+\Delta\theta_r(\omega))} : \Delta\omega = \text{cte. across } r \quad \text{(A.32)} \\
SGDC^s(\omega) &= \frac{1}{N}\sum_{r} e^{-i(\Delta\phi_r(\omega)+\Delta\theta_r(\omega))} : \Delta\omega = \text{cte. across } \omega \quad \text{(A.33)}
\end{aligned}$$

In the eqs. A.32 and A.33, $\Delta\theta_r(\omega)$ is the incremental phase associated with the random phase-shift $\theta_r(\omega)$ extracted from the surrogate DFT spectrum $X_r^s(\omega)$ of each brain region r. Let us consider two extreme cases derived from the eqs. A.30 and A.32 with $\Delta\theta_r(\omega)$ varying randomly across ω,

1 For $\Delta\phi_r(\omega) \approx cte. \implies |SGDC(r)| \approx 1 > |SGDC^s(r)| \approx 0$.
2 For $\Delta\phi_r(\omega)$ varying randomly across $\omega \implies |SGDC(r)| \approx |SGDC^s(r)| \approx 0$.

From these two extreme cases we infer that, for $\theta_r(\omega)$ varying randomly across ω, $|SGDC(r)|$ is the upper bound of $|SGDC^s(r)|$. As a consequence, for the A- and B-surrogates in general we obtain $|SGDC^s(r)| < |SGDC(r)|$. Similarly, in the case of A-surrogates computed with $\theta_r(\omega)$ varying randomly across the brain regions r, eqs. A.31 and A.33 in general produce $|SGDC^s(\omega)| < |SGDC(\omega)|$. In the particular case of the B-surrogates, at each frequency ω we add the same phase-shift value $\theta_r(\omega)$ in all the brain regions r, producing $\Delta\theta_r(\omega) =$

$\Delta\theta(\omega)\ \forall\ 1 \leq r \leq N$. As a consequence, by taking the modulus in both sides of the eq. A.33 we obtain the equivalence between the true data and the B-surrogate in terms of $|SGDC(\omega)|$,

$$\begin{aligned} |SGDC^s(\omega)| &= \left| e^{-i\Delta\theta(\omega)} \frac{1}{N} \sum_r e^{-i\Delta\phi_r(\omega)} \right| \\ &= \left| e^{-i\Delta\theta(\omega)} SGDC(\omega) \right| \\ &= |SGDC(\omega)| \end{aligned}$$

It is important to note that this equivalence between the true data and the B-surrogate in terms of $|SGDC(\omega)|$ holds only when the $SGDC(\omega)$ measure is computed on the whole time series (i.e., the non-time-resolved case). That is, if the $SGDC(\omega)$ measure is computed in a time-resolved manner around each avalanche, the equivalence between the true data and the B-surrogate in terms of $|SGDC(\omega)|$ is not longer true (see Fig. B.10F).

Appendix B. Supplementary results

Appendix B.1. Supplementary modeling results

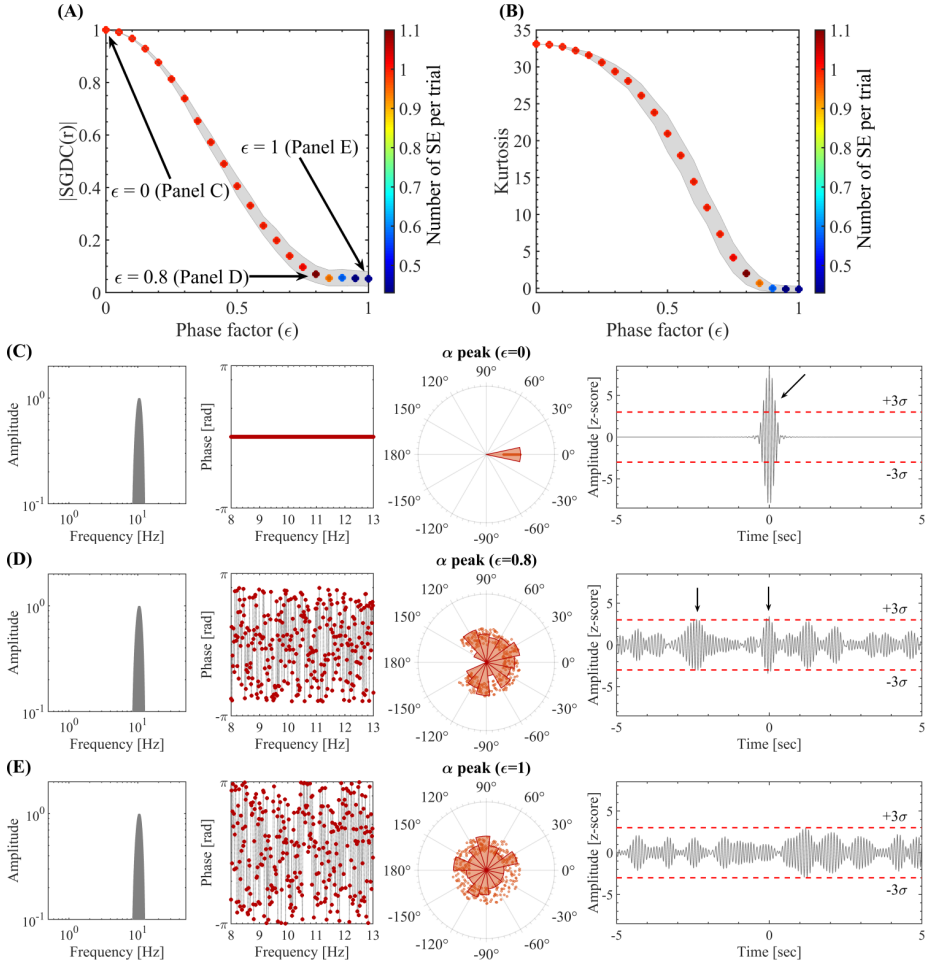

Figure B.6: Spectral group delay consistency underlies the emergence of local above-threshold fluctuations from narrowband oscillations. (A) Spectral group delay consistency, as quantified by the $SGDC(r)$ measure, as a function of the phase factor values. The colored markers indicate the mean $|SGDC(r)|$ value across 100 trials. The shaded error bars in gray correspond to the standard deviation around the mean value. The pseudocolor scale represents the mean number of SE per trial. The $SGDC(r)$ measure was obtained by computing the Equation 1 on the synthetic phase values assigned to the spectral components in the alpha band. (B) Same as in A for the Kurtosis of the amplitude values obtained by computing the Equation A.25 on the signals in time domain. (C) Amplitude spectrum (left), phase spectrum and distribution (middle), and resulting time series (right) corresponding to the signal model for a phase factor $\epsilon = 0$. For the amplitude spectrum we used a Hann window with a null-to-null bandwidth = 8-13 Hz, frequency resolution $df = 1/60\text{sec} \approx 0.017$ Hz. The phase values of the spectral components were constrained within the range $[-\epsilon\pi, \epsilon\pi]$ and disclosing a random dependence with the frequency. The black arrows in the right-most panel highlight the above-threshold fluctuations disclosed by the signal. (D) Same as in C for a phase factor $\epsilon = 0.8$. (E) Same as in C for a phase factor $\epsilon = 1$. Symbols and abbreviations: SE, Salient Events.

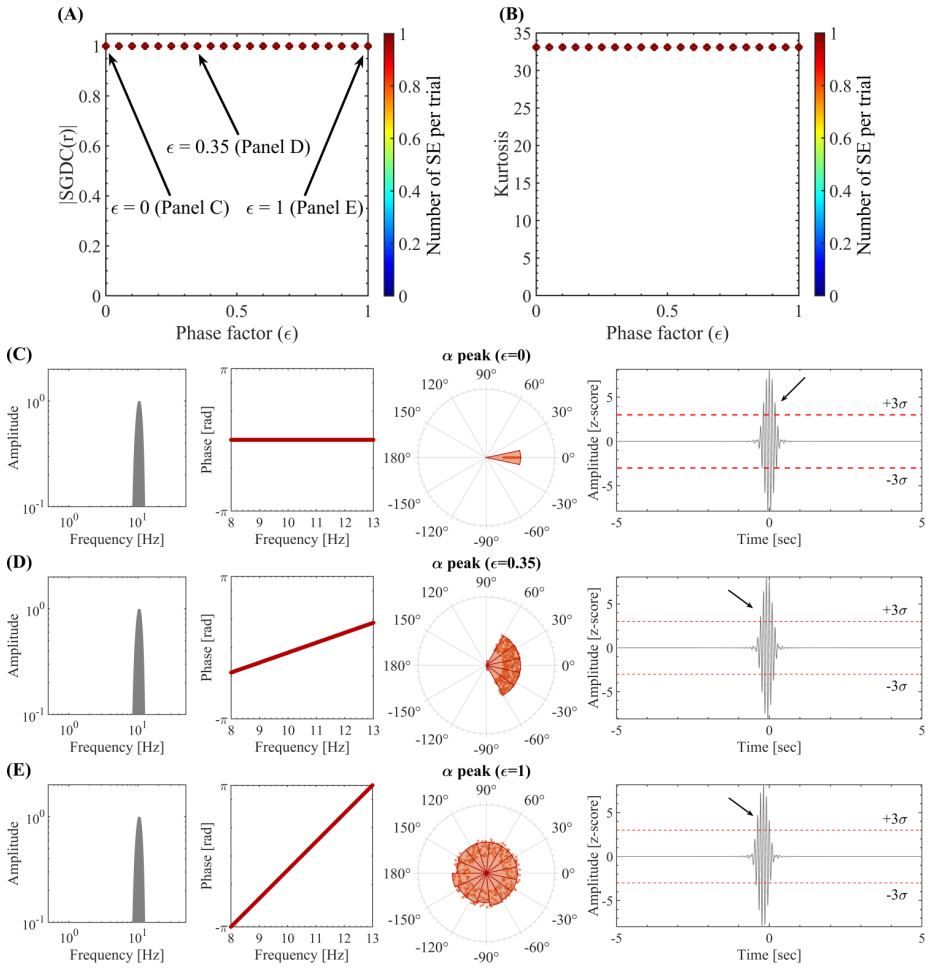

Figure B.7: Spectral group delay consistency underlies the emergence of local above-threshold fluctuations from narrowband oscillations. (A) Spectral group delay consistency, as quantified by the $SGDC(r)$ measure, as a function of the phase factor values. The colored markers indicate the mean $|SGDC(r)|$ value across 100 trials. The shaded error bars in gray correspond to the standard deviation around the mean value. The pseudocolor scale represents the mean number of SE per trial. The $SGDC(r)$ measure was obtained by computing the Equation 1 on the synthetic phase values assigned to the spectral components in the alpha band. (B) Same as in A for the Kurtosis of the amplitude values obtained by computing the Equation A.25 on the signals in time domain. (C) Amplitude spectrum (left), phase spectrum and distribution (middle), and resulting time series (right) corresponding to the signal model for a phase factor $\epsilon = 0$. For the amplitude spectrum we used a Hann window with a null-to-null bandwidth = 8-13 Hz, frequency resolution $df = 1/60\text{sec} \approx 0.017$ Hz. The phase values of the spectral components were constrained within the range $[-\epsilon\pi, \epsilon\pi]$ and disclosing a linear dependence with the frequency. The black arrows in the right-most panel highlight the above-threshold fluctuations disclosed by the signal. (D) Same as in C for a phase factor $\epsilon = 0.8$. (E) Same as in C for a phase factor $\epsilon = 1$. Symbols and abbreviations: SE, Salient Events.

Appendix B.2. Supplementary results including the deep sources

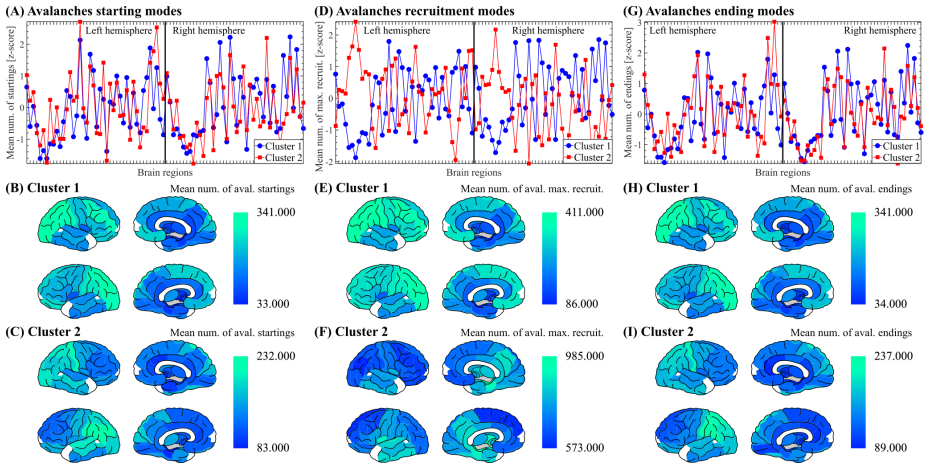

Figure B.8: Avalanches propagation modes. (A) Spatial profile for the avalanches starting modes (see Methods) corresponding to the two avalanche clusters (mean value across 41 participants). The avalanches obtained from 41 subjects were clustered using the Louvain algorithm (resolution parameter $\gamma = 1$, see Methods). The Pearson's correlation between the spatial profiles of cluster 1 and cluster 2 is $r = 0.708$, $P < 0.001$. (B) Brain topographies for the starting modes of cluster 1 avalanches as shown in panel A. (C) Brain topographies for the starting modes of cluster 2 avalanches as shown in panel A. (D-F) Same as A-B for avalanches maximum recruitment modes (see Methods). In panel D, the Pearson's correlation between the spatial profiles of cluster 1 and cluster 2 is $r = -0.841$, $P < 0.001$. (G-I) Same as A-B for avalanches ending modes (see Methods). In panel G, the Pearson's correlation between the spatial profiles of cluster 1 and cluster 2 is $r = 0.718$, $P < 0.001$. The reported P values for the statistical significance of the Pearson's correlation were assessed using Student's t distributions of the two-tailed hypothesis test under the null hypothesis that the correlation is zero.

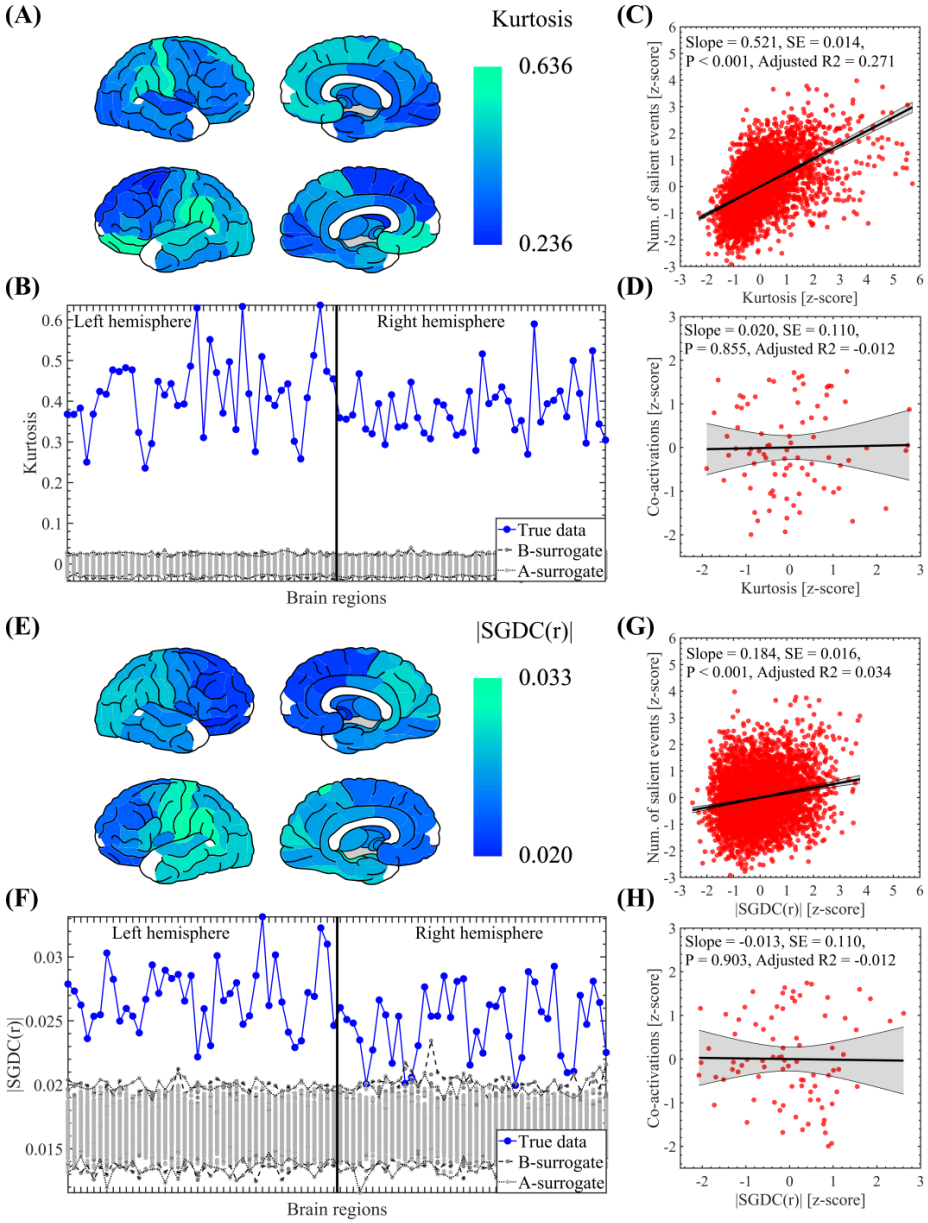

Figure B.9: Measures capturing the local salient events topographies. (A) Brain topographies for the mean kurtosis of each brain region as shown in panel B. (B) Spatial profile showing the mean kurtosis computed on the whole time series (1 min in length) of each brain region (mean value across the 47 participants, see Methods). (C) Scatter plot showing the correlation between the number of salient events and kurtosis spatial profile. Number of samples (red circles) = Number of brain regions × Number of patients = $84 \times 47 = 3948$. The thick black line and black shaded error bars represent the linear regression and the 95% confidence interval, respectively. (D) Scatter plot showing the correlation between the co-activation (Figure 6B) and kurtosis (panel B) spatial profiles. Number of samples (red circles) = Number of brain regions = 84. The thick black line and black shaded error bars represent the linear regression and the 95% confidence interval, respectively. (E-H) Same as in A-D for the $SGDC(r)$ measure. In panels C, D, G and H, the reported P values for the statistical significance of the linear regression were assessed using Student's t distributions of the two-tailed hypothesis test under the null hypothesis that the correlation is zero.

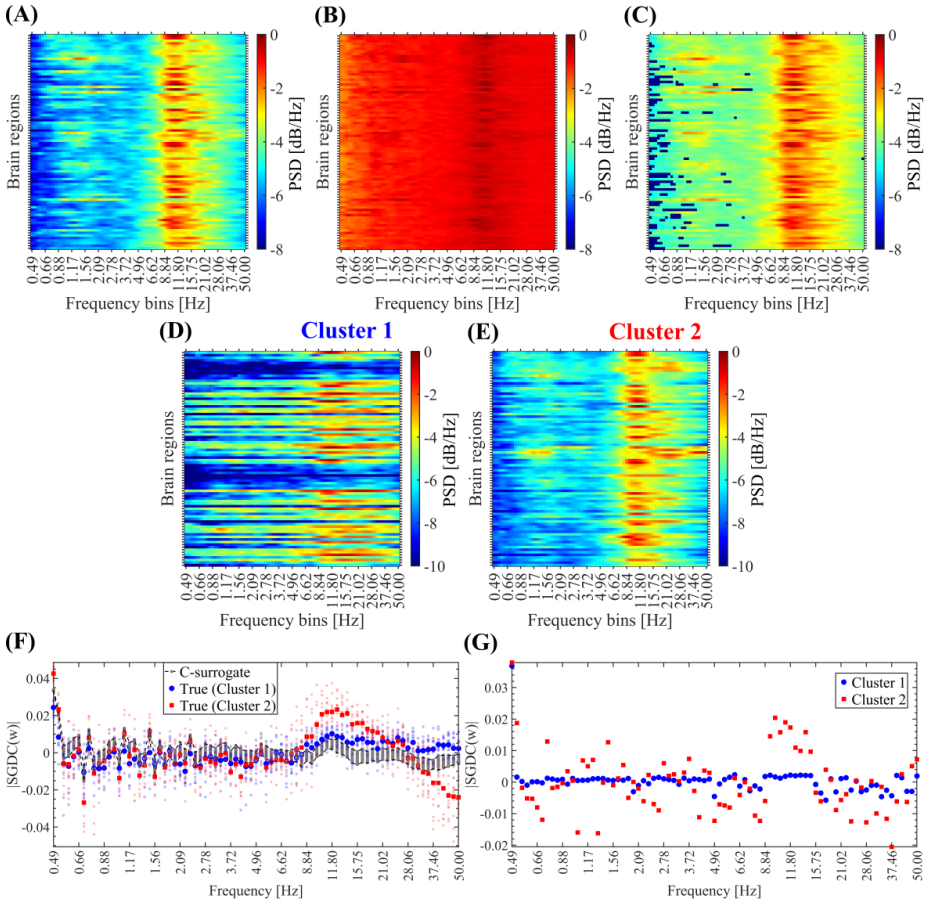

Figure B.10: Transient cross-regional coherence around the alpha band is mainly associated with neuronal avalanches. (A) Mean ASM resulting from the average across the true avalanches detected in 10 participants. (B) Mean ASM resulting from the average across the C-surrogate avalanches (see Methods) computed based on the true avalanches shown in panel A. (C) Mean ASM of the true avalanches shown in panel A thresholded with the mean ASM of the C-surrogate avalanches shown in panel B (see Methods). (D, E) Mean ASM of the two avalanches clusters identified by the Louvain algorithm computed on the avalanches detected in the 10 participants. (F) Transient cross-regional coherence quantified by the $SGDC(\omega)$ measure (see Appendix A.3), associated with the two avalanche clusters shown in panels D and E. The $SGDC(\omega)$ measure was computed in a time-resolved manner around each detected avalanche by considering the time interval corresponding to the avalanche duration (see Methods). The small markers represent mean $|SGDC(\omega)|$ values averaged across the avalanches in each individual participant. The big markers represent mean $|SGDC(\omega)|$ values averaged across the 10 participants. (G) Same as in F for the synthetic data corresponding to the large-scale model. Symbols and abbreviations: ASM, Avalanche Spectral Matrix.

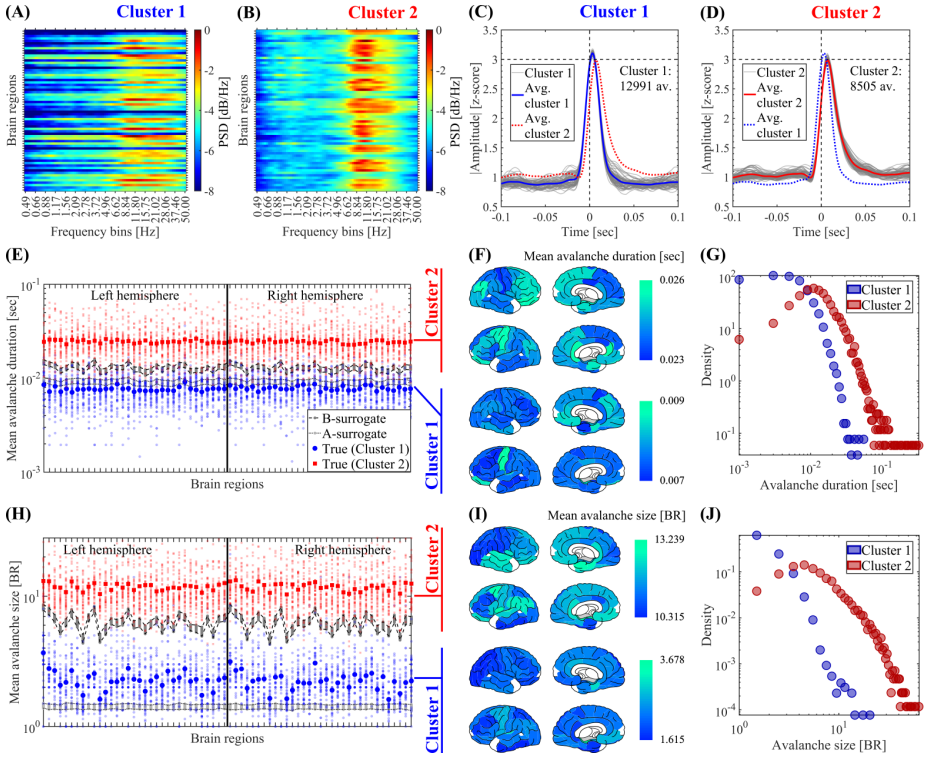

Figure B.11: Clustering of avalanches according to spectral signature. The avalanches obtained from 45 subjects were clustered using the Louvain algorithm (resolution parameter $\gamma = 1$, see Methods). (A, B) Mean ASM of the two avalanches clusters identified by the Louvain algorithm computed on the avalanches detected in the 45 participants. (C, D) Waveform shapes of the avalanches pertaining to the two avalanches clusters identified by the Louvain algorithm. Thin gray lines correspond to the average waveform shape in each brain region. Thick blue and red lines correspond to the resulting waveform shape averaged across the brain regions for avalanche cluster 1 and 2, respectively. (E) Spatial profile showing the mean duration of avalanches pertaining to cluster 1 (in blue) and cluster 2 (in red). For the true data, the small and big markers correspond to the mean spatial profile in each patient and the average across the 45 participants, respectively (see Methods). To test the significance of the difference of the mean avalanches duration between cluster 1 and cluster 2, in each brain region we computed a non-parametric permutation test (random sampling without replacement, 1×10^4 permutations). All the brain regions disclosed a statistically significant difference of the mean avalanches duration between cluster 1 and 2 (the Bonferroni-adjusted two-tailed P values result $P < 0.001$ in all the brain regions). (F) Brain topographies for the mean duration of neuronal avalanches averaged across the 45 participants as shown in panel E. (G) Distribution of the duration of avalanches pertaining to the cluster 1 and cluster 2 observed in the 45 participants. (H) Same as in E for the size of neuronal avalanches. To test the significance of the difference of the mean avalanches size between cluster 1 and cluster 2, in each brain region we computed a non-parametric permutation test (random sampling without replacement, 1×10^4 permutations). All the brain regions disclosed a statistically significant difference of the mean avalanches size between cluster 1 and 2 (the Bonferroni-adjusted two-tailed P values result $P < 0.001$ in all the brain regions). (I) Same as in F for the size of neuronal avalanches. (J) Same as in G for the size of neuronal avalanches. Symbols and abbreviations: BR, Brain Regions.

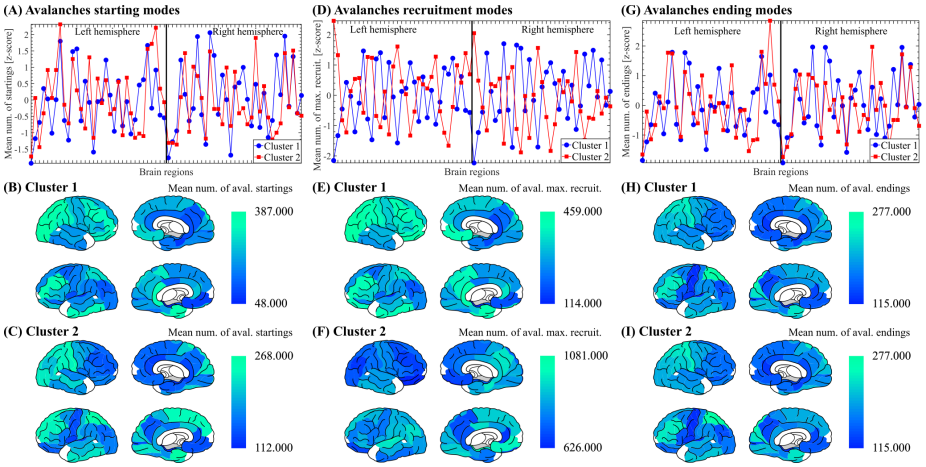

Figure B.12: Avalanches propagation modes. (A) Spatial profile for the avalanches starting modes corresponding to the two avalanche clusters (mean value across 41 participants). The avalanches obtained from 45 subjects were clustered using the Louvain algorithm (resolution parameter $\gamma = 1$, see Methods). The Pearson's correlation between the spatial profiles of cluster 1 and cluster 2 is $r = 0.584$, $P < 0.001$. (B) Brain topographies for the starting modes of cluster 1 avalanches as shown in panel A. (C) Brain topographies for the starting modes of cluster 2 avalanches as shown in panel A. (D-F) Same as A-B for avalanches maximum recruitment modes (see Methods). In panel D, the Pearson's correlation between the spatial profiles of cluster 1 and cluster 2 is $r = -0.842$, $P < 0.001$. (G-I) Same as A-B for avalanches ending modes (see Methods). In panel G, the Pearson's correlation between the spatial profiles of cluster 1 and cluster 2 is $r = 0.571$, $P < 0.001$. The reported P values for the statistical significance of the Pearson's correlation were assessed using Student's t distributions of the two-tailed hypothesis test under the null hypothesis that the correlation is zero.